Quaternary Science Reviews 283 (2022) 107461

Contents lists available at ScienceDirect

Quaternary Science Reviews

journal homepage: www.elsevier.com/locate/quascirev

New cosmogenic nuclide constraints on Late Glacial and Holocene glacier fluctuations in the sub-Antarctic Indian Ocean (Kerguelen Islands, 49°S)

Joanna Charton [a, *], Irene Schimmelpfennig [a], Vincent Jomelli [a], Guillaume Delpech [b], Pierre-Henri Blard [c], Régis Braucher [a], Deborah Verfaillie [a, d], Vincent Favier [e], Vincent Rinterknecht [a], Hugues Goosse [d], Xavier Crosta [f], Léo Chassiot [g], Léo Martin [h], Damien Guillaume [i], Claude Legentil [j], ASTER Team [k, 1]

[a] Aix Marseille Univ, CNRS, IRD, INRAE, CEREGE, Aix-en-Provence, France
[b] Université Paris-Saclay, CNRS, GEOPS, France
[c] Université de Lorraine, CNRS, CRPG, France
[d] Earth and Life Institute, Université catholique de Louvain, Louvain-la-Neuve, Belgium
[e] Institut des Géosciences de l'Environnement, Université Grenoble Alpes, CNRS, Grenoble, France
[f] UMR CNRS 5805 EPOC, Université de Bordeaux, France
[g] Université Laval, Département de Géographie, Québec, Canada
[h] Faculty of Geosciences, Utrecht University, Utrecht, the Netherlands
[i] Univ Lyon, UJM-Saint-Etienne, UCBL, ENSL, CNRS, LGL-TPE UMR5276, France
[j] Université Paris 1 Panthéon-Sorbonne, CNRS Laboratoire de Géographie Physique, France
[k] Aix Marseille Univ, CNRS, IRD, INRAE, CEREGE, Aix-en-Provence, France

ARTICLE INFO

Article history:
Received 26 December 2021
Received in revised form
27 February 2022
Accepted 15 March 2022
Available online xxx

Handling Editor: C. O'Cofaigh

Keywords:
Glacier fluctuations
Paleoclimate
^{36}Cl CRE dating
$_{10}$Be CRE dating
Late glacial
Antarctic cold reversal
Holocene
Southern mid-latitudes
Sub-Antarctic
Kerguelen islands

ABSTRACT

Cosmogenic nuclide dating of glacial landforms on the Kerguelen Archipelago (49°S, 69°E) gives the opportunity to study multi-millennial glacier fluctuations within the sub-Antarctic sector of the Indian Ocean. We here dated such geomorphic features to provide time constraints over the last 17,000 years using *in situ*-produced ^{36}Cl in three glacial valleys: Val Travers valley, Ampere Glacier valley and Arago Glacier valley. For the first time, a combination of *in situ*-produced ^{36}Cl and ^{10}Be dating and ^{26}Al/^{10}Be ratios analysis was performed in the quartz-bearing syenite boulders of the Arago Glacier site. In addition, a Bayesian approach was computed to obtain a better constraint on moraine dating. Glacial advances occurred during the Late Glacial at 16.0 ± 1.9 ka and at 12.9 ± 1.7 ka in Val Travers, and at 13.6 ± 1.8 ka in Arago Glacier valley, probably linked to the Heinrich Stadial 1 and/or Antarctic Cold Reversal events, respectively. This suggests that all glaciers at this latitude were broadly sensitive to the large-scale climatic signal of the Antarctic Cold Reversal. So far, no Early nor Mid-Holocene moraines have been found in the glacial valleys on Kerguelen, indicating that the glaciers had probably receded significantly during these periods. This is in agreement with previously determined ^{14}C ages from peat bogs, which suggest extensive deglaciation during several millennia of the Holocene period. Samples from glacially-polished bedrock surfaces (ranging from ~4.4 ka to ~14 ka) at Ampere Glacier site also suggest that this valley was ice free for several millennia during the Holocene. Finally, glaciers seem to have re-advanced only during the Late Holocene, especially within the last millennium, at ~1 ka, ~ 430 yr and ~300 yr. A comparison of this new dataset with the available ^{10}Be ages from other southern mid-latitude regions during the Holocene allows the identification of three different glacier evolution patterns. We suspect that variations of Kerguelen glaciers, which are located in the Southern Indian Ocean, were controlled by the combined effects of sea surface temperature related to the variations of the Antarctic Polar Front and fluctuations of precipitation related to long-term variations of the Southern Annular Mode.

* Corresponding author.
E-mail address: charton@cerege.fr (J. Charton).
[1] ASTER Team: Georges Aumaître, Didier Bourlès (†), Karim Keddadouche.

https://doi.org/10.1016/j.quascirev.2022.107461
0277-3791/

1. Introduction

Reconstruction of the long-term evolution of glacier fluctuations provides the opportunity to better understand their sensitivity to multi-millennial and -centennial climate change, in particular to the variability of air temperature and precipitation. Cosmic ray exposure (CRE) dating of glacio-geomorphologic formations, such as moraines, erratic boulders and glacially-eroded bedrock, using *in situ*-produced cosmogenic nuclides is particularly suited to reconstruct past glacier chronologies (Balco et al., 2020). Most paleoglacier records in the mid-latitudes of the Southern Hemisphere are based on the well-constrained *in situ* ^{10}Be dating method applied to quartz-bearing moraine boulders (e.g. Putnam et al., 2012; Reynhout et al., 2019). In only few studies moraine chronologies are established from the less commonly used *in situ* ^{36}Cl and ^{3}He (Eaves et al., 2019; Rudolph et al., 2020). A consistent glacier evolution has been evidenced in various regions of the mid-latitudes of the Southern Hemisphere during the Holocene (11.7 ka - present) with glaciers located in New Zealand (e.g. Putnam et al., 2012), South Georgia (e.g. Bakke et al., 2021) and Patagonia (e.g. Reynhout et al., 2019) experiencing their maximal Holocene extent during the Early Holocene (11.6–8 ka), followed by a gradual decrease of glacier extent throughout time. This multi-millennial trend is attributed to the variation in summer insolation (Putnam et al., 2012) and at an intra-millennial scale to variations in precipitation intensity (Reynhout et al., 2019; Bakke et al., 2021). However, two additional contrasting patterns of glacier fluctuations have been observed recently. In the Darwin Cordillera (southernmost Patagonia), Reynhout et al. (2021) provided the first ^{10}Be moraine chronology that shows a maximum Holocene extent during the last millennium corroborating the radiocarbon-dating-based results from previous studies by Hall et al. (2019), while on the Antarctic Peninsula, a maximal glacier advance was recorded during the Mid-Holocene (8–4 ka; Kaplan et al., 2020).

These asynchronous fluctuation patterns challenge the concept of a homogeneous Holocene glacier evolution within the southern mid-latitudes and raise the question whether regional rather than hemispheric climatic variations have driven glacier behavior during the Holocene. While CRE glacial paleorecords are increasingly numerous in Patagonia and New Zealand, the knowledge on glacier fluctuations in other parts of the southern mid-latitudes remains fragmented. To fill this gap, the Kerguelen Archipelago (49°S, 69°E) provides a precious sentinel in the Southern Indian Ocean to reconstruct glacier evolution (Fig. 1). Indeed, Kerguelen is the largest still glaciated sub-Antarctic archipelago of the southern mid-latitudes (Favier et al., 2016), where several terrestrial moraines are preserved and can be dated. Therefore, establishing a meaningful glacier chronology at Kerguelen is of major interest, as it improves our knowledge of glacier fluctuations at the regional southern mid-latitudes scale within the larger scope of the Southern Hemisphere.

Existing studies on Kerguelen glaciers document their fluctuations from Marine Isotopic Stage 3 (MIS-3; 60–25 ka) to the last millennium (section 2.2; Jomelli et al., 2017, 2018; Charton et al., 2020; Verfaillie et al., 2021). However, knowledge of the evolution of glaciers at Kerguelen from the end of the Late Glacial

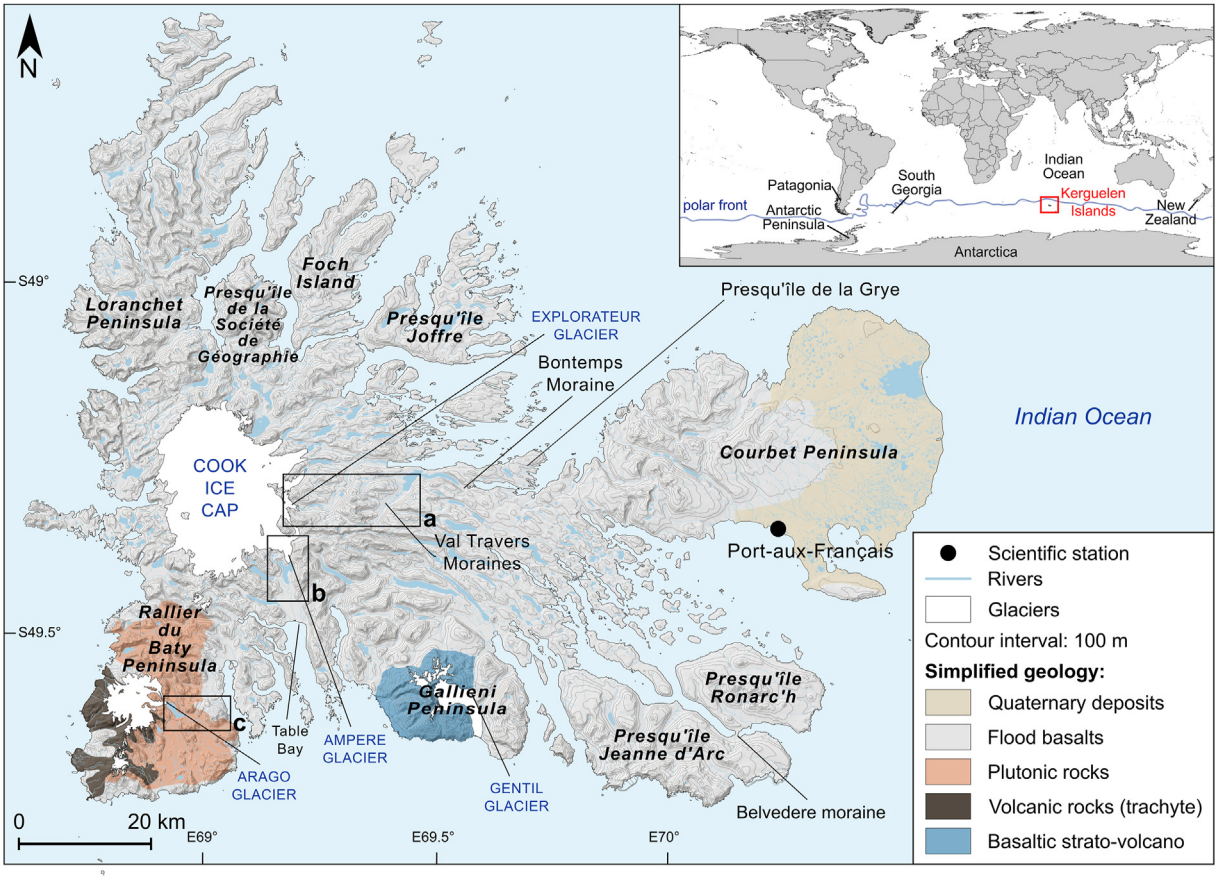

Fig. 1. Map of the Kerguelen Archipelago with the relevant geology in a simplified form. The inset shows its location in the Southern Indian Ocean. The three study areas are framed in black, **a.** Val Travers site, **b.** Ampere Glacier site, **c.** Arago Glacier site, for which geomorphological maps are presented in Figs. 4, 6 and 7, respectively. (data: Digital Elevation Model from NASA/METI/AIST/Japan Spacesystems and U.S./Japan ASTER Science Team, 2019; glacier outlines from the GLIMS database (Raup et al., 2007); geological units from Ponthus (2018)).

(19.0–11.7 ka) to the Late Holocene (4–0 ka) remains limited. Several discrete radiocarbon ages from peatland (Frenot et al., 1997) revealed by modern recession of the Ampere Glacier suggest that this glacier was at least as small as it is currently during several millennia of the Holocene. Therefore, the aim of this study is to address the paucity of Late Glacial and Holocene glacier constraints at Kerguelen, using ^{36}Cl CRE dating on samples of all lithologies, complemented by ^{10}Be and ^{26}Al CRE analyses on quartz-bearing syenite samples. To do so, we targeted glacial landforms whose position and glacial context in the landscape may provide information on Late Glacial and Holocene glacier fluctuations (section 2.3). Based on the combination of these two dating methods and a Bayesian approach explained in section 3, we provide an updated Kerguelen glacier chronology spanning from the Late Glacial to the last millennium (sections 4 and 5.1), which is explored in the context of the other glacier and climate records from the southern mid-latitudes (sections 5.2 and 5.3.).

2. Study area and geomorphological setting

The Kerguelen Archipelago is located in the Southern Indian Ocean, with a total surface area of 7215 km^2. These 30-million-year-old islands constitute the emerging part of the large underwater basaltic Kerguelen Plateau (Giret et al., 2003, Fig. 1). However, the regional geology varies and the basaltic crust is locally intruded by plutonic rocks of various compositions, such as on the Rallier du Baty Peninsula, where a large volcano-plutonic complex contains Qz-bearing syenites, or in the Galliéni Peninsula, which comprises a young volcano-plutonic complex of less than 1 Ma. The eastern part of the Courbet Peninsula is also different and is only characterized by quaternary deposits but no flood basalts (Fig. 1).

2.1. Climate setting

Due to its location in the Southern Indian Ocean, the Kerguelen Archipelago is subjected to a subpolar oceanic climate. The related moist and cool air masses, transported by the Southern Westerly Winds (SWW), enabled the formation of ice caps and glaciers. The SWW also drives the Antarctic Circumpolar Current (ACC). The ACC flows eastward between 45°S and 65°S (Sokolov and Rintoul, 2009) and is affected by the bathymetry of the Kerguelen Plateau (46–63°S, 62–85°E). Kerguelen is located in between the sub-Antarctic Front (SAF) at ~ 46°S (Solokov and Rintoul, 2009) and the Antarctic Polar Front (APF) at ~ 50°S (Park et al., 2014). Nowadays, Kerguelen receives an average of 800 mm of precipitation per year and the mean annual temperature is about 4.5 °C at sea level, as recorded daily since 1951 at the scientific station of Port-aux-Français (Courbet Peninsula; Fig. 1). Additional observations have provided information on the spatial variability of the climate in the archipelago (Verfaillie et al., 2015; Favier et al., 2016). In particular, a strong foehn effect has been identified, being responsible for five times more precipitation in the western part than in the eastern part of the archipelago (Verfaillie et al., 2019).

2.2. Previous studies on glaciers and their fluctuations at Kerguelen

The western part of the main Kerguelen island, Grande Terre, hosts the warm-based Cook Ice Cap (CIC; 1050 m a.s.l.), which covered ~ 400 km^2 in 2020 (Verfaillie et al., 2021). Several other smaller glaciated areas are also located on the Rallier du Baty

Fig. 2. a. Photograph of Val Travers site showing V2 moraine and the bedrock surface. **b.** shows a view of Ampere proglacial margin towards Table Bay presenting the sampled paired bedrock surfaces and perched erratic boulders. **c.** and **d.** are photographs of A1 moraine and A2b moraine, respectively, located on Arago Glacier forefield.

Peninsula in the southwest of the archipelago, on the Gallieni Peninsula in the south, and on the Presqu'île de la Société de Géographie north of CIC (Fig. 1).

Previous studies on Kerguelen based on ^{36}Cl dating of glacial features revealed that glaciers began to retreat at ~41 ka ago (Jomelli et al., 2018). Erratic and bedrock surfaces located farther inland of the island dated to ~29–24 ka suggest that large expanses of ice were still present at that time. Glaciers receded probably until about 15 ka ago. The general glacier recession during the Late Glacial period was interrupted likely during the Antarctic Cold Reversal (ACR; 14.5–12.9 ka), as indicated by ^{36}Cl dating of three moraines at different locations – *i.e.* the Bontemps moraine at 13.6 ± 1.5 ka, Belvedere moraine at 15.5 ± 1.8 ka and G1 moraine of Gentil glacier at 14.3 ± 2.3 ka (Jomelli et al., 2017, 2018; Charton et al., 2020). A Late Holocene advance is recorded on the debris-covered Gentil Glacier at 2.62 ± 0.97 ka, located at the base of Mount Ross (the highest summit on Kerguelen, 1850 m a.s.l.) (Charton et al., 2020). Finally, ^{36}Cl ages from moraines deposited by Ampere Glacier, an outlet glacier of CIC, reveal - albeit with some scatter - the occurrence of at least two advances of the Ampere Glacier during the last millennium (Jomelli et al., 2017; Verfaillie et al., 2021). One is attributed to the beginning of the Little Ice Age (Solomina et al., 2016), and used to constrain a glaciological model that simulated the extent of the Cook Ice Cap during this period (Verfaillie et al., 2021).

Since the 1960s, glaciers at Kerguelen have experienced dramatic wastage, with the surface area of the CIC expected to disappear by 2100 CE (Verfaillie et al., 2021). This is explained by decreasing precipitation mainly attributed to the high index Southern Annular Mode (SAM+) (Thompson et al., 2011; Verfaillie et al., 2015; Favier et al., 2016) and to the long-term increase in atmospheric temperatures (Verfaillie et al., 2021). Mass and energy balance conducted on the CIC reveals that temperature impacts the precipitation phase and the equilibrium line altitude, through changes in the elevation of the 0 °C isotherm and therefore of the rain/snow limit with impacts on both the snow accumulation amount and the glacier surface albedo (Favier et al., 2016).

2.3. Study sites and sampling strategy

Three sites hosting datable geomorphological features (i.e. moraines, glacially-polished bedrock and erratics) that are estimated to belong to the Late Glacial and/or the Holocene, based on a comparison with existing data elsewhere on the islands, were chosen: the Val Travers valley, Ampere Glacier and Arago Glacier (Fig. 1). Moraines were labelled with numbers in ascending order from the oldest to the youngest.

The Val Travers site (Fig. 1) is characterized by extended U-shaped valleys that were incised into the basaltic substratum by the eastern outlet glaciers of the CIC. It lies about 10 km upstream of Bontemps Lake (Fig. 4). We sampled the only two preserved terrestrial moraines found in the valley (V1 and V2), which may have been formed by a branch of the Explorateur Glacier (Fig. 4). Four samples (VLT-10, -11, −12, and −13) were taken at 62 m a.s.l from the V1 moraine ridge, which is located at 14.2 km from the present-day frontal area of the eastern glaciers of the CIC (Fig. 4). Five moraine boulders (VLT-05, -06, −07, −08, and −09) were sampled at 73 m a.s.l. on the V2 moraine, which was deposited about 1.5 km upstream of the V1 moraine (Figs. 2a and 4). Finally, one sample (VLT-04) was extracted from a polished bedrock surface, located on the right-lateral plateau near Mount A. Gampert at an elevation of 437 m a.s.l. and at a distance of about 9 km downstream of the V1 moraine (Figs. 2a and 4). All boulders sampled at this site have a basaltic lithology.

The Ampere Glacier is a lake-terminating outlet glacier of the CIC, which flows south-east of the ice cap on the basaltic substratum (Fig. 1). Currently, the Ampere Glacier (67 km^2 in 2011) is 12 km long (Berthier et al., 2009; Verfaillie et al., 2021) with a large proglacial lake. The Ampere's proglacial margin (9 km long) is characterized by an outwash plain that reaches Table Bay, with a set of six moraines between about 3.5 and 7 km from the current ice front (Figs. 1 and 6). Eleven new basaltic samples, i.e. six erratic boulders (MO-03, -04, −06, −08, −11, and −12) and five bedrock samples (MO-02, -05, −07, −09, and −13) were taken uphill (between 120 and 290 m a.s.l.) on the southern part of the shore of the Ampere Lake at distances ranging from 1.5 to 2.8 km from the glacier's snout (Figs. 2b and 6). Each sampled bedrock surface is paired with at least one erratic (Figs. 2b and 6). These erratic boulders are aligned in a lateral continuum of the frontal moraine sequence.

The south-west part of the archipelago hosts the Rallier du Baty Peninsula (Fig. 1), an alkaline volcano-plutonic complex, which mostly consists of syenites with rock crystallization ages ranging from about 12 Ma to 8 Ma (Ponthus et al., 2020). More recent lava flows, composed of trachytes, are also present, resulting from volcanic activity between ~1.15 Ma (Dosso et al., 1979) and the last millennium (900–1000 CE) (Guillaume Delpech, personal communication). Rallier du Baty Peninsula is covered by a small ice cap, with several land-terminating outlet glaciers. Among them, the Arago Glacier, which peaks at 1262 m a.s.l., is a 6 km long lake-terminating glacier and flows down on the eastern slope of Mont Henri, towards the east into the Larmor valley (Figs. 1 and 7). The only moraine (A1) so far detected at a distal location (11 km) from the current glacier front, is composed of syenite boulders. Six syenite samples (RDB-23, -24, −25, −26, −27, and −28) were taken at 72 m a.s.l. on this outermost A1 moraine (Figs. 2c and 7). Closer to the glacier front, a sequence of four moraines mainly composed of volcanic rocks (trachyte) was identified, but only two of them (the most distant from the current front) were chosen for dating: A2a and A2b (Fig. 7). They were formed alongside the moraine-damned lake at about 3 km from the current glacier front. From the crest of the frontal moraine A2a, four samples (RDB-01, -02, −04, and −05) were taken at 80 m a.s.l., all being syenites (Fig. 7). Another three samples of trachytic composition (RDB-15, -17, and −18) were collected from the ridge of the lateral moraine A2b at 157 m a.s.l. (Figs. 2d and 7). In addition, one glacially-polished syenite bedrock sample (RDB-13) was taken at an average elevation of 60 m a.s.l. on the right-lateral flank of the valley, located at about 5 km upstream of A1 moraine (Fig. 7).

3. Methods

3.1. Sampling

Sampling was carried out during a field campaign in 2017–2018. In total, 34 samples from glacially-polished bedrock, moraine boulders and erratic boulders were collected (Table 1). A hammer and chisel were used to extract the uppermost 2–3 cm of moraine boulder surfaces, erratic boulders and bedrock (Fig. 2). Particular attention was paid to sample flat and non-weathered surfaces. The geographic coordinates and elevations were recorded with a handheld GPS device and topographic shielding was measured in the field with a clinometer.

3.2. In situ cosmogenic nuclide dating

For CRE dating *in situ* ^{36}Cl is the most suitable cosmogenic nuclide, because Kerguelen's volcanic lithology contains Ca, K, Ti, Fe, and Cl, which are the main target elements for analysis with this method. We also conducted ^{10}Be measurements on samples that

Table 1
Geographic sample locations, topographic shielding factors, sample thicknesses, and formation age of rock.

Sample Name	Latitude (°S)	Longitude (°E)	Elevation (m)	Shielding factor	Thickness (cm)	Lithology	Formation age of rock	Mineral used for CRE dating
Val Travers Valley								
Glacially polished bedrock								
VLT-04	49.32255	69.47100	437	0.998	3	Basalt	25 Ma[a]	whole rock for ^{36}Cl
V1 moraine								
VLT-10	49.33952	69.38428	63	0.998	3	Basalt	25 Ma[a]	whole rock for ^{36}Cl
VLT-11	49.33965	69.38419	61	0.988	3	Basalt	25 Ma[a]	whole rock for ^{36}Cl
VLT-12	49.33976	69.38411	67	0.988	3	Basalt	25 Ma[a]	whole rock for ^{36}Cl
VLT-13	49.34031	69.38671	57	0.988	3	Basalt	25 Ma[a]	whole rock for ^{36}Cl
V2 moraine								
VLT-05	49.34846	69.36926	75	0.984	2	Basalt	25 Ma[a]	whole rock for ^{36}Cl
VLT-06	49.34827	69.36966	72	0.998	3	Basalt	25 Ma[a]	whole rock for ^{36}Cl
VLT-07	49.34845	69.37011	74	0.998	3	Basalt	25 Ma[a]	whole rock for ^{36}Cl
VLT-08	49.34832	69.37067	72	0.984	3	Basalt	25 Ma[a]	whole rock for ^{36}Cl
VLT-09	49.34834	69.37077	72	0.998	3	Basalt	25 Ma[a]	whole rock for ^{36}Cl
Ampere Glacier								
Glacially polished bedrocks								
MO-13	49.42739	69.18063	123	0.998	2	Basalt	25 Ma[a]	whole rock for ^{36}Cl
MO-05	49.42353	69.17365	148	0.994	3	Basalt	25 Ma[a]	whole rock for ^{36}Cl
MO-02	49.42207	69.17475	141	0.994	3	Basalt	25 Ma[a]	whole rock for ^{36}Cl
MO-09	49.41459	69.17542	280	0.966	3	Basalt	25 Ma[a]	whole rock for ^{36}Cl
MO-07	49.41459	69.17514	293	0.994	3	Basalt	25 Ma[a]	whole rock for ^{36}Cl
Erratic boulders								
MO-12	49.42739	69.18063	123	0.998	2	Basalt	25 Ma[a]	whole rock for ^{36}Cl
MO-11	49.42751	69.18103	122	0.998	2	Basalt	25 Ma[a]	whole rock for ^{36}Cl
MO-04	49.42345	69.17365	147	0.994	3	Basalt	25 Ma[a]	whole rock for ^{36}Cl
MO-03	49.42253	69.17473	141	0.994	3	Basalt	25 Ma[a]	whole rock for ^{36}Cl
MO-08	49.41459	69.17542	287	0.994	3	Basalt	25 Ma[a]	whole rock for ^{36}Cl
MO-06	49.41459	69.17514	293	0.994	2	Basalt	25 Ma[a]	whole rock for ^{36}Cl
Arago Glacier								
A1 moraine								
RDB-23	49.62756	69.06640	68	0.985	3	Syenite	9 Ma[b]	felspars for ^{36}Cl
RDB-24	49.62759	69.06632	72	0.985	5	Syenite	9 Ma[b]	felspars for 36Cl, quartz for 10Be and 26Al
RDB-25	49.62759	69.06648	72	0.985	3	Syenite	9 Ma[b]	felspars for ^{36}Cl
RDB-26	49.62777	69.06668	70	0.985	3	Syenite	9 Ma[b]	felspars for ^{36}Cl
RDB-27	49.62795	69.06667	74	0.985	3	Syenite	9 Ma[b]	felspars for ^{36}Cl, quartz for ^{10}Be and ^{26}Al
RDB-28	49.62794	69.06678	72	0.985	3	Syenite	9 Ma[b]	felspars for ^{36}Cl
Glacially polished bedrocks								
RDB-13	49.64710	69.00906	54	0.995	3	Syenite	9 Ma[b]	quartz for ^{10}Be and ^{26}Al
A2a moraine								
RDB-01	49.61876	68.98058	80	0.989	3	Syenite	10 ka[c]	felspars for ^{36}Cl
RDB-02	49.61859	68.98078	77	0.989	3	Syenite	10 ka[c]	felspars for ^{36}Cl
RDB-04	49.61844	68.98085	77	0.989	3	Syenite	10 ka[c]	whole rock for ^{36}Cl
RDB-05	49.62082	68.97874	84	0.993	3	Syenite	10 ka[c]	felspars for ^{36}Cl
A2b moraine								
RDB-15	49.62007	68.96879	146	0.998	3	Trachyte	10 ka[c]	whole rock for ^{36}Cl
RDB-17	49.61993	68.96826	157	0.989	3	Ignimbrite trachyte	10 ka[c]	whole rock for ^{36}Cl
RDB-18	49.61990	68.96792	156	0.989	3	Ignimbrite trachyte	10 ka[c]	whole rock for ^{36}Cl

[a] Annell (2005); Nicolaysen et al. (2000).
[b] Ponthus (2018).
[c] Guillaume Delpech (personal communication).

allowed the isolation of sufficient quartz. In addition, we measured ^{26}Al in these samples with the aim to verify if the sampled surfaces have been affected by some inheritance from the last interglacial (long-term exposure-burial) or by recent exhumation.

3.2.1. Chemical procedures

Sample preparation for *in situ*-produced ^{36}Cl, ^{10}Be and ^{26}Al CRE dating was performed in the "Laboratoire National des Nucléides Cosmogéniques" (LN_2C) at CEREGE, Aix-en-provence, France. Samples were crushed and sieved to collect the 250–500 μm fraction.

All samples but one (RDB-13) presented in this study were dated with ^{36}Cl. Basaltic and trachytic whole-rock samples were processed according to routine procedures using a method similar to Schimmelpfennig et al. (2011). The low abundance of phenocrysts in these rocks required the use of the whole-rock fractions for these samples, as in the previous studies in the Kerguelen Islands (Jomelli et al., 2017, 2018; Charton et al., 2020; Verfaillie et al., 2021). Aliquots of bulk rocks were selected for analyses of major and trace element concentrations at the Service d'Analyze des Roches et des Minéraux (SARM, Nancy, France) (Table 2). Major and trace elements are needed to evaluate the contribution of the capture of low-energy neutrons on ^{35}Cl and the nucleogenic production to the total ^{36}Cl production. Exposure dating of syenites from Rallier du Baty represented a considerable experimental effort, as they have never been processed before for ^{36}Cl or other cosmogenic nuclides at the LN_2C laboratory. All syenite samples are dominated by alkali feldspars (Na and K-rich) with minor amounts of quartz and other magnetic minerals (mainly amphiboles and pyroxenes). Because the feldspars were expected to have low amounts of natural Cl and

Table 2
Chemical compositions of the bulk rock samples before chemical treatment. Analysis performed at the SARM-CRPG (Nancy, France) by ICP-OES (major elements), ICP-MS (trace element), atomic absorption (Li), colorimetry (B) and spectrophotometry (Cl).

Sample Name	CaO %	K_2O %	TiO_2%	Fe_2O_3%	Cl (ppm)	SiO_2%	Na_2O %	MgO %	Al_2O_3%	MnO %	P_2O_5%	CO_2%	Li (ppm)	B (ppm)	Sm (ppm)	Gd (ppm)	Th (ppm)	U (ppm)	LOI
Val Travers Valley																			
Glacially polished bedrock																			
VLT-04	10.49	0.56	1.57	9.59	60	46.64	2.72	4.26	19.64	0.14	0.21	1.15	6.43	2.1	4.49	4.48	1.23	0.25	4.08
V1 moraine																			
VLT-10	10.63	0.52	2.29	12.14	83	47.05	2.67	4.74	15.75	0.16	0.29	–	4.3	3.3	5.70	5.55	1.73	0.42	3.56
VLT-11	10.45	0.48	2.37	12.52	85	46.75	2.60	4.97	14.80	0.15	0.29	0.83	3.87	3.9	5.77	5.53	1.80	0.44	4.24
VLT-12	10.58	0.45	2.37	12.43	95	46.66	2.61	4.95	15.01	0.17	0.3	0.97	4.04	3.4	6.95	6.69	1.80	0.45	4.18
VLT-13	10.85	0.64	2.13	11.49	70	47.74	2.80	4.29	17.43	0.14	0.27	1.61	4.99	2.6	4.34	4.27	1.60	0.37	2.27
V2 moraine																			
VLT-05	10.17	0.66	2.53	13.02	52	47.59	2.91	4.40	15.97	0.17	0.36	–	5.75	3.4	5.70	5.55	1.97	0.45	1.89
VLT-06	10.17	0.66	2.53	13.02	52	47.59	2.91	4.40	15.97	0.17	0.36	–	5.75	3.4	5.70	5.55	1.97	0.45	1.89
VLT-07	11	0.56	1.84	10.57	37	47.41	2.85	4.31	18.46	0.14	0.25	–	5.79	2.8	4.44	4.38	1.37	0.30	2.55
VLT-08	10.17	0.66	2.53	13.02	52	47.59	2.91	4.40	15.97	0.17	0.36	–	5.75	3.4	5.70	5.55	1.97	0.45	1.89
VLT-09	9.35	0.75	3.22	15.48	67	47.77	2.98	4.49	13.49	0.21	0.47	–	5.71	4	7	6.71	2.58	0.60	1.23
Ampere Glacier																			
Glacially polished bedrock																			
MO-13	9.68	0.32	3.02	13.60	48	45.07	2.58	5.59	13.95	0.19	0.37	–	7.5	3	6.86	6.76	2.38	0.55	3.85
MO-05	9.68	0.32	3.02	13.60	48	45.07	2.58	5.59	13.95	0.19	0.37	–	7.5	3	6.86	6.76	2.38	0.55	3.85
MO-02	10.20	0.35	2.73	13.04	48	45.31	2.62	6.05	14.11	0.19	0.29	0.53	7.50	3	5.24	5.32	1.73	0.39	4.13
MO-09	9.17	0.3	3.30	15.66	50	44.82	2.53	5.13	13.79	0.19	0.45	–	6.65	2	8.48	8,21	3.04	0.70	3.58
MO-07	9.68	0.32	3.02	13.60	48	45.07	2.58	5.59	13.95	0.19	0.37	–	7.5	3	6.86	6.76	2.38	0.55	3.85
Erratic boulders																			
MO-12	8.24	0.98	2.70	14.51	90	50.4	2.99	4.24	13.26	0.19	0.42	–	6.53	3.72	7.50	7.21	2.90	0.67	1.66
MO-11	6.87	1.34	2.42	18.14	73	51.57	2.72	3.17	11.35	0.18	0.29	0.93	9.27	3.8	5.68	5.64	2.26	0.48	1.43
MO-04	9.32	0.66	3.22	14.78	91	49.04	3.06	4.82	13.17	0.2	0.42	–	4.83	4.4	7.14	6.91	2.46	0.58	0.98
MO-03	8.24	0.98	2.70	14.51	90	50.4	2.99	4.24	13.26	0.19	0.42	–	6.53	3.72	7.50	7.21	2.90	0.67	1.66
MO-08	6.10	1.92	2.59	12.26	73	53.9	3.54	2.97	13.48	0.18	0.72	–	9.66	4.2	12.37	11.59	5.23	1.24	1.78
MO-06	10.96	0.29	2.26	11.90	36	47.74	2.54	6.12	15.26	0.18	0.23	–	4.7	2.5	4.57	4.48	1.41	0.34	1.94
Arago Glacier																			
A1 moraine																			
RDB-23	1.10	6.57	0.72	4.24	185	62.79	5.95	0.45	17.18	0.11	0.14	–	7.98	2	6.05	4.61	1.6	1	2.41
RDB-24	2.09	5.72	1.32	9.03	155	57.84	5.17	0.86	15.24	0.29	0.39	0.35	4.90	3.3	16.30	12.30	2.6	1.23	1.94
RDB-25	1.98	6.05	1.2	7.43	230	59.47	5.37	0.86	15.67	0.2	0.35	0.49	10.00	3.1	14	10.69	2.6	1.23	0.99
RDB-26	0.72	6.98	0.44	2.42	150	64.43	6.1	0.22	18.11	0.06	–	–	2.52	2	2.94	2.29	3.72	1.29	1.62
RDB-27	1.14	6.40	0.61	4.24	170	62.91	6.07	0.43	16.93	0.11	0.15	–	6.95	2	8.40	6.28	2.6	1.23	0.53
RDB-28	1.55	6.98	0.87	6.71	120	60.9	5.72	0.6	16.14	0.16	0.35	–	9.83	2	13.71	10.19	7.97	1.38	1.62
A2a moraine																			
RDB-01	2.75	0.03	0.08	8.46	80	44.2	0.24	39.09	3.33	0.13	< L.D.	0.31	13.3	4.3	0.2	0.3	2.6	1.23	0.51
RDB-02	1.17	5.78	0.51	5	45	63.29	6.32	0.31	16.34	0.15	0.08	0.55	12.7	3.8	6.30	4.79	2.6	1.23	0.63
RDB-04	2.20	6.58	1,09	4.84	120	59.69	5.20	0.87	16.33	0.15	0.39	–	10.5	2	14.08	10.72	7.20	1.84	2.94
RDB-05	1.16	5.76	0.51	5.03	95	63.33	6.36	0.29	16.36	0.14	0.08	0.96	13.3	4.0	6.2	4.71	2.6	1.23	0.83
A2b moraine																			
RDB-15	1.18	5.75	0.56	5.30	63	63.54	6.26	0.34	15.99	0.16	–	–	15.5	2.5	8.23	6.19	12.83	2.53	0
RDB-17	1.25	5.81	0.53	5.01	46	63.36	6.32	0.31	16.26	0.15	–	–	12.1	4	7.08	5.29	10.77	1.6	0.37
RDB-18	1.25	5.81	0.53	5.01	46	63.36	6.32	0.31	16.26	0.15	–	–	12.1	4	7.08	5.29	10.77	1.6	0.37

they are the dominant non-magnetic mineral phase, they were separated for chemical ^{36}Cl extraction from the magnetic minerals in the syenite samples (RDB-01, -02, −05, −23, −24, −25, −26, −27 and −28) using a Frantz magnetic separator. We then leached all samples with a HF/HNO_3 (Ultrapur) acid mixture with the aim to eliminate atmospheric ^{36}Cl and other potentially Cl-rich mineral phases (Schimmelpfennig et al., 2009). This step removed ~10–20% of the initial feldspar-dominated fractions and ~40% of the initial whole rock sample. Another 2 g aliquot of the rinsed and dried grains for each sample was sent to SARM for major element analyses by ICP-OES, which provides the concentrations of the target elements (*i.e.* Ca, K, Ti and Fe) for ^{36}Cl production by spallation and slow muon capture (Table 3). The final dissolution of the sample grains was performed in a HF/HNO_3 (Ultrapur) acid mixture after addition of a ^{35}Cl-enriched spike (~99%) for isotope dilution (Ivy-Ochs et al., 2004). In total, 6 chemistry blanks (Bk 5, Bk 7, Bk 8, Bk 10, Bk 11 and Bk 12) were processed together with the samples (one with each sample batch, see Table 4 for detailed information). The remaining steps follow the method presented in Schimmelpfennig et al. (2011). Prior to AMS measurements, AgCl targets were pressed into nickel cathodes. $^{36}Cl/^{35}Cl$ and $^{35}Cl/^{37}Cl$ ratio measurements were performed by Accelerator Mass Spectrometry (AMS) at the French AMS national facility (ASTER) after normalization to the inhouse standard SM-CL-12, using an assigned value of 1.428 (±0.021) x 10^{-12} for the $^{36}Cl/^{35}Cl$ ratio (Merchel et al., 2011) and assuming a natural ratio of 3.127 for the stable ratio $^{35}Cl/^{37}Cl$. From these measurements the ^{36}Cl and Cl concentrations were calculated, using the principles of isotope dilution and following the equations in Schimmelpfennig (2009). All concentrations were blank-corrected by subtracting the number of atoms Cl and ^{36}Cl of the batch-specific blank from those of the corresponding samples, respectively (Table 4). An error propagation calculation was performed following the standard procedures given in Taylor (1997).

All syenite samples were inspected for the amount of quartz they contained. Eight samples were estimated to have at least 1% of quartz, which was isolated from the magnetic minerals by magnetic separation (using a Frantz magnetic separator) and from K-feldspars by densimetric separation using heavy liquids. The quartz fraction was leached several times using a diluted HF acid mixture in an ultrasonic bath to remove any remaining feldspars and to eliminate atmospheric ^{10}Be from the quartz grains. Finally, only three samples

Table 3
Concentrations of the major element oxides, determined in splits taken from the samples after the chemical pre-treatment (acid etching). Analysis performed at the SARM-CRPG (Nancy, France) by ICP-OES.

Sample Name	CaO %	K_2O %	TiO_2%	Fe_2O_3%	SiO_2%	Na_2O %	MgO %	Al_2O_3%	MnO %	P_2O_5%	LOI
Val Travers Valley											
Glacially polished bedrock											
VLT-04	10.58 ± 0.21	0.66 ± 0.13	2.34 ± 0.23	10.32 ± 0.21	51.6 ± 1.0	2.86 ± 0.29	3.82 ± 0.38	16.29 ± 0.33	0.153 ± 0.031	< L.D. (0.10)	1.08
V1 moraine											
VLT-10	11.04 ± 0.22	0.37 ± 0.09	3.15 ± 0.31	10.16 ± 0.20	53.32 ± 1.07	2.64 ± 0.26	4.72 ± 0.47	13.23 ± 0.26	0.18 ± 0.036	< L.D. (0.10)	0.59
VLT-11	11.03 ± 0.22	0.51 ± 0.10	3.25 ± 0.33	9.88 ± 0.99	52.1 ± 1.0	2.69 ± 0.27	4.34 ± 0.43	14.00 ± 0.28	0.166 ± 0.033	< L.D. (0.10)	1.06
VLT-12	11.07 ± 0.22	0.48 ± 0.12	3.24 ± 0.32	9.85 ± 0.99	52.4 ± 1.0	2.71 ± 0.27	4.41 ± 0.44	14.00 ± 0.28	0.183 ± 0.037	< L.D. (0.10)	1.02
VLT-13	10.70 ± 0.21	0.69 ± 0.14	2.78 ± 0.28	10.12 ± 0.20	51.4 ± 1.0	2.72 ± 0.27	4.14 ± 0.41	15.18 ± 0.30	0.160 ± 0.032	< L.D. (0.10)	1.1
V2 moraine											
VLT-05	10.55 ± 0.21	0.74 ± 0.15	2.69 ± 0.27	10.11 ± 0.20	51.99 ± 1.04	2.89 ± 0.29	4.05 ± 0.41	15.46 ± 0.31	0.17 ± 0.034	< L.D. (0.10)	0.3
VLT-06	10.95 ± 0.22	0.69 ± 0.14	2.82 ± 0.28	9.68 ± 0.97	52.04 ± 1.04	2.99 ± 0.30	4.13 ± 0.41	15.63 ± 0.31	0.15 ± 0.03	< L.D. (0.10)	0.64
VLT-07	11.15 ± 0.22	0.64 ± 0.13	2.57 ± 0.26	8.85 ± 0.88	52.33 ± 1.05	2.94 ± 0.29	3.87 ± 0.39	16.42 ± 0.33	0.15 ± 0.03	< L.D. (0.10)	0.62
VLT-08	11.18 ± 0.22	0.60 ± 0.12	2.30 ± 0.23	9.09 ± 0.91	51.13 ± 1.02	2.85 ± 0.29	3.52 ± 0.35	17.58 ± 0.35	0.15 ± 0.03	< L.D. (0.10)	0.7
VLT-09	9.06 ± 0.45	0.81 ± 0.16	3.93 ± 0.39	13.95 ± 0.28	51.82 ± 1.04	2.94 ± 0.29	4.27 ± 0.43	12.48 ± 0.25	0.21 ± 0.042	< L.D. (0.10)	0
Ampere Glacier											
Glacially polished bedrocks											
MO-13	9.17 ± 0.46	0.37 ± 0.09	3.76 ± 0.38	13.67 ± 0.27	53.17 ± 1.06	2.46 ± 0.25	5.23 ± 0.10	11.45 ± 0.23	0.23 ± 0.046	< L.D. (0.10)	0.46
MO-05	9.21 ± 0.46	0.37 ± 0.09	3.19 ± 0.32	12.06 ± 0.24	55.57 ± 1.11	2.19 ± 0.22	5.72 ± 0.11	10.05 ± 0.20	0.21 ± 0.042	< L.D. (0.10)	1.61
MO-02	10.68 ± 0.21	0.358 ± 0.090	3.02 ± 0.30	9.89 ± 0.99	52.9 ± 1.1	2.821 ± 0.28	5.15 ± 0.10	13.09 ± 0.26	0.155 ± 0.031	0.180 ± 0.027	1.78
MO-09	10.16 ± 0.20	0.23 ± 0.06	5.57 ± 0.56	14.50 ± 0.29	49.58 ± 0.99	2.23 ± 0.22	5.76 ± 0.12	10.44 ± 0.21	0.24 ± 0.048	< L.D. (0.10)	–
MO-07	8.06 ± 0.40	0.68 ± 0.14	3.90 ± 0.39	14.67 ± 0.29	52.72 ± 1.05	2.78 ± 0.28	4.41 ± 0.44	11.71 ± 0.23	0.23 ± 0.046	< L.D. (0.10)	1.01
Erratic boulders											
MO-12	5.96 ± 0.30	1.08 ± 0.11	3.37 ± 0.34	13.44 ± 0.27	55.55 ± 1.11	3.59 ± 0.36	3.47 ± 0.35	11.09 ± 0.22	0.15 ± 0.03	< L.D. (0.10)	1.91
MO-11	5.27 ± 0.26	1.44 ± 0.14	2.88 ± 0.29	14.56 ± 0.29	57.9 ± 1.2	2.63 ± 0.26	2.88 ± 0.29	8.64 ± 0.86	0.157 ± 0.031	< L.D. (0.10)	2.43
MO-04	8.79 ± 0.44	0.69 ± 0.14	3.77 ± 0.38	14.12 ± 0.28	52.43 ± 1.05	2.95 ± 0.30	4.82 ± 0.48	12.02 ± 0.24	0.21 ± 0.042	< L.D. (0.10)	0
MO-03	6.95 ± 0.35	0.43 ± 0.11	2.41 ± 0.24	12.59 ± 0.25	56.53 ± 1.13	3.13 ± 0.31	4.39 ± 0.44	7.90 ± 0.79	0.19 ± 0.038	0.20 ± 0.03	5.12
MO-08	4.27 ± 0.64	2.07 ± 0.21	3.13 ± 0.31	10.49 ± 0.21	62.09 ± 1.24	3.39 ± 0.34	1.86 ± 0.19	11.89 ± 0.24	0.19 ± 0.038	< L.D. (0.10)	0.05
MO-06	10.30 ± 0.21	0.30 ± 0.08	3.06 ± 0.31	11.61 ± 0.23	53.86 ± 1.08	2.08 ± 0.21	6.21 ± 0.12	11.01 ± 0.22	0.21 ± 0.042	< L.D. (0.10)	0.93
Arago Glacier											
A1 moraine											
RDB-23	0.30 ± 0.07	6.92 ± 0.35	0.03 ± 0.01	0.16 ± 0.03	67.36 ± 1.35	6.27 ± 0.32	< L.D. (0.03)	18.48 ± 0.37	< L.D. (0.015)	< L.D. (0.10)	0.79
RDB-24	0.41 ± 0.10	7.15 ± 0.36	0.051 ± 0.013	0.174 ± 0.034	67.3 ± 1.4	6.53 ± 0.33	< L.D. (0.03)	19.06 ± 0.38	< L.D. (0.015)	< L.D. (0.10)	0.84
RDB-25	0.41 ± 0.10	7.35 ± 0.37	0.051 ± 0.013	0.209 ± 0.042	67.3 ± 1.4	6.289 ± 0.31	< L.D. (0.03)	18.91 ± 0.38	< L.D. (0.015)	< L.D. (0.10)	0.86
RDB-26	0.35 ± 0.09	6.74 ± 0.34	0.04 ± 0.01	0.13 ± 0.03	66.74 ± 1.33	6.56 ± 0.33	< L.D. (0.03)	18.68 ± 0.37	< L.D. (0.015)	< L.D. (0.10)	0.64
RDB-27	0.24 ± 0.06	7.17 ± 0.36	0.04 ± 0.01	0.26 ± 0.05	66.01 ± 1.32	6.57 ± 0.33	< L.D. (0.03)	18.70 ± 0.37	< L.D. (0.015)	< L.D. (0.10)	1.06
RDB-28	0.26 ± 0.07	7.01 ± 0.35	0.04 ± 0.01	0.20 ± 0.04	66.90 ± 1.34	6.47 ± 0.32	< L.D. (0.03)	18.62 ± 0.37	< L.D. (0.015)	< L.D. (0.10)	0.51
A2a moraine											
RDB-01	1.16 ± 0.17	5.95 ± 0.30	0.50 ± 0.10	3.70 ± 0.37	64.8 ± 1.3	6.45 ± 0.32	0.253 ± 0.051	16.76 ± 0.34	0.097 ± 0.019	< L.D. (0.10)	0.44
RDB-02	1.18 ± 0.18	5.90 ± 0.30	0.51 ± 0.10	3.93 ± 0.39	64.4 ± 1.3	6.43 ± 0.32	0.273 ± 0.055	16.63 ± 0.33	0.105 ± 0.021	< L.D. (0.10)	0.05
RDB-04	0.61 ± 0.09	7.10 ± 0.36	1.25 ± 0.12	3.51 ± 0.35	63.38 ± 1.27	5.63 ± 0.28	0.19 ± 0.038	17.33 ± 0.35	0.09 ± 0.018	< L.D. (0.10)	1.95
RDB-05	1.16 ± 0.17	5.81 ± 0.29	0.51 ± 0.10	4.05 ± 0.41	64.2 ± 1.3	6.44 ± 0.32	0.265 ± 0.053	16.54 ± 0.33	0.107 ± 0.021	< L.D. (0.10)	0.84
A2b moraine											
RDB-15	1.16 ± 0.17	5.95 ± 0.30	0.51 ± 0.05	3.49 ± 0.35	65.06 ± 1.30	6.54 ± 0.33	0.27 ± 0.054	16.99 ± 0.34	0.09 ± 0.018	< L.D. (0.10)	0
RDB-17	1.17 ± 0.18	6.03 ± 0.30	0.43 ± 0.11	3.07 ± 0.31	64.79 ± 1.30	6.38 ± 0.32	0.24 ± 0.048	17.07 ± 0.34	0.08 ± 0.016	< L.D. (0.10)	0.19
RDB-18	1.23 ± 0.19	5.84 ± 0.29	0.48 ± 0.12	3.68 ± 0.37	65.14 ± 1.30	6.40 ± 0.32	0.28 ± 0.056	16.93 ± 0.34	0.09 ± 0.018	< L.D. (0.10)	0

Table 4
^{36}Cl dating results. Spike is enriched in ^{35}Cl (~99.9%). $^{36}Cl/^{35}Cl$ and $^{35}Cl/^{37}Cl$ ratios were inferred from measurements at the AMS facility ASTER. Samples in italic were rejected as outliers and excluded from mean age calculations.

Sample Name	Sample weight (g)	mass of Cl in spike (mg)	$^{35}Cl/^{37}Cl$	$^{36}Cl/^{35}Cl$ (10^{-14})	[Cl] in sample (ppm)	[^{36}Cl] (10^3 atoms g^{-1})	Age (yr)[a]	Arithmetic mean age (yr)	Chi^2 test
Val Travers Valley									
Glacially polished bedrock									
VLT-04	40.49	2.004	19.62 ± 0.86	13.35 ± 0.90	11.5	133.2 ± 9.1	17,300 ± 2200 (1700)	–	–
V1 moraine									
VLT-10	36.99	2.006	24.55 ± 0.78	6.30 ± 0.49	9.1	64.7 ± 5.2	12,600 ± 1700 (1300)	16,000 ± 1900[c]	Accepted
VLT-11	37.4	2.009	24.05 ± 1.36	8.10 ± 0.61	9.6	84.6 ± 6.5	16,000 ± 2100 (1600)		Accepted
VLT-12	36.93	2.021	31.13 ± 1.64	8.47 ± 0.67	7.1	87.2 ± 6.9	16,700 ± 2200 (1700)		Accepted
VLT-13	40.33	2.003	23.11 ± 1.70	8.26 ± 0.66	9.4	80.2 ± 6.5	14,900 ± 2000 (1600)		Accepted
V2 moraine									
VLT-05	48.64	2.015	17.58 ± 0.29	9.82 ± 0.75	7.5	83.7 ± 6.4	15,600 ± 2000 (1600)	12,900 ± 1700[c]	Accepted
VLT-06	43.13	2.004	20.50 ± 0.82	7.55 ± 0.58	9.9	68.8 ± 5.4	12,400 ± 1600 (1300)		Accepted

(*continued on next page*)

Table 4 (*continued*)

Sample Name	Sample weight (g)	mass of Cl in spike (mg)	$^{35}Cl/^{37}Cl$	$^{36}Cl/^{35}Cl$ (10^{-14})	[Cl] in sample (ppm)	[^{36}Cl] (10^3 atoms g^{-1})	Age (yr)[a]	Arithmetic mean age (yr)	Chi^2 test
VLT-07	42.79	2.010	22.78 ± 0.44	7.58 ± 0.49	8.7	68.5 ± 4.6	12,400 ± 1500 (1200)		Accepted
VLT-08	46.19	2.001	17.57 ± 0.64	10.02 ± 0.60	7.8	89.3 ± 5.4	16,700 ± 2000 (1500)		Accepted
VLT-09	42.63	2.009	15.71 ± 0.46	7.35 ± 0.45	14.3	71.9 ± 4.6	13,500 ± 1700 (1300)		Accepted
Ampere Glacier									
Glacially polished bedrocks									
MO-13	58.27	2.005	71.10 ± 2.84	8.69 ± 0.72	1.2	52.0 ± 4.4	11,300 ± 1600 (1300)	–	–
MO-05	71.76	1.992	51.63 ± 1.85	13.04 ± 0.73	1.7	64.5 ± 3.7	14,000 ± 1800 (1300)	–	–
MO-02	51.40	2.006	9.84 ± 0.20	6.40 ± 0.50	23	60.2 ± 4.9	10,100 ± 1300 (1000)	–	–
MO-09	70.77	2.019	71.83 ± 1.50	4.85 ± 0.39	0	24.4 ± 2.0	4430 ± 590 (450)	–	–
MO-07	61.49	2.003	46.30 ± 2.25	8.26 ± 0.58	2.3	47.9 ± 3.5	8900 ± 1100 (940)	–	–
Erratic boulders									
MO-12	57	2.006	30.37 ± 0.59	0.412 ± 0.078	4.4	1.60 ± 0.60	290 ± 140 (140)	610 ± 250	Accepted
MO-11	75.87	2.004	13.67 ± 0.56	0.84 ± 0.14	9.9	4.72 ± 0.80	870 ± 180 (180)		Accepted
MO-04	*88.06*	*1.989*	*5.73 ± 0.15*	*0.401 ± 0.026*	*35.3*	*2.65 ± 0.32*	*80 ± 50 (50)*		*Rejected*
MO-03	46.71	2.012	12.70 ± 0.21	0.52 ± 0.14	17.6	4.2 ± 1.4	680 ± 340 (340)		Accepted
MO-08	74.54	2.007	7.47 ± 0.47	1.04 ± 0.13	24.9	7.3 ± 1.1	620 ± 170 (170)		Accepted
MO-06	*54.97*	*2.010*	*55.03 ± 0.94*	*2.17 ± 0.25*	*2.1*	*13.6 ± 1.6*	*2370 ± 380 (330)*		*Rejected*
Arago Glacier									
A1 moraine									
RDB-23	47	2.022	4.438 ± 0.073	8.26 ± 0.60	134.4	203.3 ± 17.0	13,700 ± 2000 (1500)	13,600 ± 1800	Accepted
RDB-24	99.47	2.009	3.794 ± 0.067	10.18 ± 0.71	124.5	197.6 ± 21.6	14,100 ± 2200 (1900)		Accepted
RDB-25	99.55	2.011	3.538 ± 0.062	8.95 ± 0.64	202.4	263.4 ± 39.9	15,400 ± 3100 (2800)		Accepted
RDB-26	47.87	2.030	4.666 ± 0.077	8.17 ± 0.63	112.8	177.6 ± 15.1	11,600 ± 1700 (1400)		Accepted
RDB-27	*63.67*	*1.981*	*4.112 ± 0.075*	*6.56 ± 0.51*	*129.7*	*144.2 ± 14.1*	*9200 ± 1400 (1200)*		*Rejected*
RDB-28	52.35	2.009	5.269 ± 0.088	10.22 ± 0.68	73.1	163.0 ± 11.7	13,300 ± 1600 (1400)		Accepted
A2a moraine									
RDB-01	83.56	2.013	5.013 ± 0.092	0.91 ± 0.12	52.1	8.7 ± 1.4	760 ± 150 (140)	1120 ± 330	Accepted
RDB-02	79.91	2.006	6.29 ± 0.12	1.72 ± 0.21	32.1	13.3 ± 1.8	1380 ± 230 (220)		Accepted
RDB-04	*93.94*	*2.010*	*3.932 ± 0.70*	*1.75 ± 0.26*	*109.2*	*30.6 ± 5.1*	*2250 ± 440 (410)*		*Rejected*
RDB-05	69.54	2.005	5.41 ± 0.19	1.21 ± 0.17	51.5	12.6 ± 2.1	1210 ± 230 (220)		Accepted
A2b moraine									
RDB-15	61.53	2.029	6.22 ± 0.11	0.56 ± 0.11	43.2	5.66 ± 1.25	480 ± 120 (120)	300 ± 170	Accepted
RDB-17	59.87	2.004	10.80 ± 0.57	0.369 ± 0.097	17.1	1.86 ± 0.83	170 ± 90 (80)		Accepted
RDB-18	71.63	2.012	6.69 ± 0.13	0.401 ± 0.056	31.8	2.67 ± 0.56	230 ± 60 (60)		Accepted
Blanks[b]					**Total atoms Cl (10^{17})**	**Total atoms ^{36}Cl (10^4)**			
Bk5	–	2.013	170.3 ± 4.0	0.294 ± 0.076	3.63 ± 0.46	10.2 ± 2.6	–	–	–
Bk7	–	1.988	233.5 ± 10.8	0.037 ± 0.019	1.31 ± 0.32	12.7 ± 6.4	–	–	–
Bk8	–	1.990	165.5 ± 4.8	0.190 ± 0.049	3.84 ± 0.26	6.5 ± 1.7	–	–	–
Bk10	–	1.938	41.1 ± 0.8	0.042 ± 0.020	31.11 ± 0.92	1.51 ± 0.70	–	–	–
Bk11	–	2.029	200.3 ± 5.9	0.113 ± 0.036	2.37 ± 0.22	4.0 ± 1.3	–	–	–
Bk12	–	2.010	195.1 ± 3.5	0.132 ± 0.043	2.54 ± 0.14	3.9 ± 1.5	–	–	–

[a] Age uncertainties are reported at 1 sigma level and were calculated through full propagation of analytical and production rate errors. Numbers in brackets are analytical uncertainties only.

[b] Bk5 was processed with the samples RDB-01, -02, −05, −24, −25 and MO-02. Bk7 was processed with VLT-04, -11, −12, −13 and MO-11. Bk8 was processed with MO-04, -05, 07, −08, −12, −13, VLT-06, -07, −09, −10, RDB-17 and -18. Bk10 was processed with MO-09, VLT-05 and -08. Bk11 was processed with RDB-15, and -27. Bk12 was processed with RDB-23, -26, −28, −04, MO-03 and -06.

[c] This corresponds to the median age due to the bayesian filtering.

(RDB-13, -24 and −27) yielded sufficient amounts of quartz for ^{10}Be and ^{26}Al chemical procedures (~12–52 g from at least 4 kg of crushed rock). As RDB-13 was collected from a quartz-enriched vein, it yielded the highest amount of quartz (~52 g). The total dissolution of the samples was then performed in a concentrated HF solution after the addition of 150 μl of an in-house ^{9}Be carrier solution (3025 ± 9 ppm; Merchel et al., 2008). An aliquot of the solution was taken after complete digestion of the samples to quantify the total Al concentration by ICP-OES analysis. Due to the presence of high amounts of natural ^{27}Al in the processed fraction (probably due to small residues of feldspars), no ^{27}Al carrier was added to the aliquot. Beryllium and aluminum were extracted using anion and cation exchange columns and alkaline precipitation. Afterwards, samples were oxidized at 700 °C for 1 h and the final BeO and Al_2O_3 were mixed with niobium and silver powders respectively, and loaded into copper cathodes. AMS measurements of the $^{10}Be/^{9}Be$ ratios were

Table 5
AMS analytical data, ^{10}Be exposure ages and ^{26}Al/^{10}Be ratios. ^{10}Be/^{9}Be and ^{26}Al/^{27}Al ratios were inferred from measurements at the ASTER AMS facility. The numbers in brackets correspond to the internal (analytical) uncertainty at 1σ level.

Sample name	Quartz weight (g)	mass of carrier (^{9}Be mg)	^{10}Be/^{9}Be (10^{-14})	[^{10}Be] (10^{4} atoms g^{-1})	^{10}Be exposure ages (ka)	^{26}Al/^{27}Al (10^{-14})	Total ^{27}Al (ppm)	[^{26}Al] (10^{4} atoms g^{-1})	^{26}Al/^{10}Be
Arago Glacier: A1 moraine									
RDB-24	15.7	0.45611	3.94 ± 0.19	7.42 ± 0.38	16.25 ± 0.83 (0.82)	0.46 ± 0.23	853.31	6.8 ± 3.4	0.91 ± 0.46
RDB-27	12.62	0.68822	1.474 ± 0.095	5.08 ± 0.35	11.00 ± 0.75 (0.75)	4.24 ± 0.61	375.06	47.8 ± 6.9	9.4 ± 1.4
Arago glacier: glacially polished bedrock									
RDB-13	51.99	0.46307	9.79 ± 0.35	5.76 ± 0.21	12.53 ± 0.46 (0.44)	22.1 ± 2.1	75.93	37.3 ± 3.6	6.48 ± 0.64

Chemistry blank data

Blank name	mass of carrier (^{9}Be mg)	^{10}Be/^{9}Be (10^{-14})	[^{10}Be] (10^{4} atoms)
BL-01	0.45611	0.121 ± 0.023	3.70 ± 0.70

conducted at the French national AMS facility (ASTER) (Arnold et al., 2010). Samples were calibrated against the in-house standard STD-11 (^{10}Be/^{9}Be = 1.191 ± 0.013 × 10^{-11}; Braucher et al., 2015) and using a ^{10}Be half-life of 1.387 (±0.0012) x 10^{6} years (Chmeleff et al., 2010; Korschinek et al., 2010). Aluminum measurements were performed against an in-house standard SM-Al-11 with ^{26}Al/^{27}Al = (7.401 ± 0.064) x 10^{-12} which has been cross-calibrated against the primary standards certified by a round-robin exercise (Merchel and Bremser, 2004). Analytical uncertainties include ASTER counting statistics and stability, the latter amounting to ~0.5% for ^{10}Be (Arnold et al., 2010). ^{10}Be measurements were corrected for blank background by subtracting the number of atoms ^{10}Be of the blank from those of the samples (Table 5).

3.2.2. CRE age calculations

The ^{36}Cl CRE age calculations were performed using the Excel® spreadsheet published by Schimmelpfennig et al. (2009), following the methods used in the previous Kerguelen studies (Jomelli et al., 2017, 2018; Charton et al., 2020; Verfaillie et al., 2021). The calculator takes into account all ^{36}Cl production reactions (spallation of the target elements Ca, K, Ti and Fe, slow muon capture by Ca and K, capture of cosmogenic low-energy (*i.e.* thermal and epithermal) neutrons by ^{35}Cl and nucleogenic production) and provides in detail their relative contributions (Supplemental Material Table 1), based on the sea level and high latitude (SLHL) production rates, scaling factors, sample chemical composition (Tables 2 and 3), sample thickness, topographic shielding, and rock formation age (Table 1). The time-invariant "St" scaling (Stone, 2000) was used for the calculation of all samples. As no local production rates exist for the Kerguelen Archipelago, the following ^{36}Cl SLHL production rates, mostly calibrated at mid-latitude sites and previously applied in Kerguelen, were used for the calculations: 42.2 ± 4.8 atoms of ^{36}Cl (g Ca)$^{-1}$ yr^{-1} for Ca spallation (Schimmelpfennig et al., 2011), 148.1 ± 7.8 atoms of ^{36}Cl (g K)$^{-1}$ yr^{-1} for K spallation (Schimmelpfennig et al., 2014), 13 ± 3 atoms of ^{36}Cl (g Ti)$^{-1}$ yr^{-1} for spallation of Ti (Fink et al., 2000), 1.9 ± 0.2 atoms of ^{36}Cl (g Fe)$^{-1}$ yr^{-1} for Fe spallation (Stone et al., 2005), and 696 ± 185 neutrons (g air)$^{-1}$ yr^{-1} for the rate of epithermal neutron production from fast neutrons in the atmosphere at the Earth/atmosphere interface (Marrero et al., 2016). We applied a value of 160 g cm^{-2} for the high-energy neutron attenuation length and 2.4 g cm^{-3} for the bulk rock density. The two ^{36}Cl production reactions induced by capture of low-energy neutrons on ^{35}Cl are hard to quantify, as the low-energy neutron flux depends on the rock composition and environmental factors, such as snow cover and presence of water (Zreda et al., 1993; Phillips et al., 2001; Schimmelpfennig et al., 2009; Zweck et al., 2013; Dunai et al., 2014). We therefore attributed a 30% uncertainty to the ^{36}Cl production from capture of cosmogenic low-energy neutrons by ^{35}Cl reaction production, based on empirical and model experiments (Zreda et al., 1993; Schimmelpfennig et al., 2009; Zweck et al., 2013; Dunai et al., 2014; Marrero et al., 2016). The estimation of the nucleogenic ^{36}Cl contribution in the spreadsheet follows the calculations provided by Phillips and Plummer (1996). The nucleogenic ^{36}Cl production is induced by low-energy neutron capture on ^{35}Cl, but in this case the low-energy neutrons result from spontaneous fission of ^{238}U and reactions of alpha-particles generated during U and Th decay. The calculation method further assumes that nucleogenic ^{36}Cl production starts with the rock formation (crystallization) and is not preserved during magmatic processes (Gosse and Phillips, 2001; Schimmelpfennig et al., 2009; Sarıkaya et al., 2018; Anjar et al., 2021). After ~1–2 Ma, nucleogenic ^{36}Cl production and decay (half-life of ^{36}Cl: 301 ka) are in equilibrium, which makes the nucleogenic ^{36}Cl contribution sensitive to differences in the formation ages only if they are <1 Ma (Sarıkaya et al., 2018). Most rock samples in our dataset have formation ages that are much older than 1 Ma (Table 1; Guillaume Delpech, personal communication). The nucleogenic ^{36}Cl production is therefore in equilibrium with ^{36}Cl decay. Only samples from a recent lava flow on Arago Glacier site (samples RDB-01, -02, −04, −05, −15, −17 and −18) have a young formation age of ~10 ka or less (Guillaume Delpech, personal communication; Table 1), i.e. the nucleogenic ^{36}Cl contribution is much lower than in the older samples. Further, calculations of the nucleogenic ^{36}Cl production in the spreadsheet developed by Schimmelpfennig et al. (2009) are based on the assumption that the nucleogenic flux of neutrons is homogenous within the bulk rock. Thus, the bulk rock composition in U and Th is commonly used to estimate the nucleogenic production of ^{36}Cl in our samples. This assumption is valid when dating volcanic material because the fast cooling of the lava commonly induces little crystallization with the sparse occurrence of bigger phenocrysts in the matrix. In the case of Kerguelen, the basalts and trachytes used in this study are mostly aphyric or have a microlitic porphyric microstructure with only a few percent of phenocrysts. On the contrary, the plutonic syenite samples of our dataset have a coarse-grained microstructure and are composed of large crystals (up to centimeter size), frequently including small inclusions of accessory minerals (hundreds of microns or less) with highly variable U and Th concentrations (eg. zircon, monazite). It is therefore plausible that the nucleogenic neutron flux is not homogeneous in the syenites samples due to the occurrence of accessory minerals in some larger crystals. In order to prevent a bias in the estimation of the nucleogenic production for the plutonic samples, we thus used the U and Th compositions of the feldspar-dominated fractions separated instead of the U–Th concentrations of the bulk fraction because the ^{36}Cl analysis was performed on these felspar separates. We assign a formal

uncertainty of 5% to the nucleogenic ^{36}Cl production, as to our knowledge no specific investigations have been conducted on the uncertainties inherent to the commonly-used calculation approach. In the Excel® spreadsheet, all uncertainties are propagated throughout to the final ^{36}Cl exposure age following the standard procedures given in Taylor (1997).

^{10}Be CRE ages were calculated with the online CREp program (Martin et al., 2017; http://crep.crpg.cnrs-nancy.fr) and are listed in Table 5. Scaling to the sample locations was made according to the time-dependent version of the Stone (2000) scaling (Martin et al., 2017), with the ERA40 atm (Uppala et al., 2005) and the atmospheric ^{10}Be-based VDM geomagnetic database (Muscheler et al., 2005). The production rate used to compute the ^{10}Be ages is regional "southern mid-latitudes" mean based on three calibration sites located in Patagonia (Kaplan et al., 2011) and New-Zealand (Putnam et al., 2010b), as available in the online ICE-D dataset (Martin et al., 2017; http://calibration.ice-d.org/). Using the Stone time-dependent scaling in CREp, this regional mean ^{10}Be production rate corresponds to a sea level high latitude (SLHL) value of 4.05 ± 0.04 atoms g^{-1} yr^{-1}. Note that this value is only 1.5% lower than the global average computed with all available worldwide calibration sites (Martin et al., 2017).

No correction was made for snow cover nor denudation for both the ^{36}Cl and ^{10}Be age calculations, in line with previously published ^{36}Cl ages from Kerguelen. Current seasonal snow cover corresponds to a thickness of maximum 10 cm, during durations of about 1.5 months at 90 m a.s.l. and 3 weeks at 35 m a.s.l. (Verfaillie et al., 2015; Favier et al., 2016). Such cover would correspond to a correction lower than 2% (Delunel et al., 2014) and can hence be safely neglected. Similarly, given the exposure timescale (<20 ka), the impact of denudation is probably lower than the analytical uncertainties by denudation processes.

The resulting ^{36}Cl and ^{10}Be CRE ages are listed in Tables 4 and 5 with their inferred 1 σ uncertainties (*i.e.* the total uncertainties which take into account the analytical and production rate uncertainties) and their analytical uncertainties in brackets. Surface exposure ages are also plotted and shown in Figs. 4, 6 and 7. In the main text and on the figures, we indicate the individual ages with their total uncertainties, whereas probability density curves of individual ages are presented with analytical uncertainties only to allow internal comparison (Figs. 3, 5 and 9). For a given site, the obtained ages from a single object (moraine, erratic) were compared using a Chi^2 test, and 95% outliers were then removed (Ward and Wilson, 1978). Then, in line with former Kerguelen studies, we computed the arithmetic mean ^{36}Cl age for each object (reported with their total uncertainties in Table 4). All exposure ages are expressed in yr until 1 ka, and in ka for older ages.

3.3. Bayesian modeling

To reduce the dating uncertainties, we exploited the stratigraphic relationships between the dated glacial objects and applied a Bayesian filter on a part of our ^{36}Cl moraine age dataset (Cooley et al., 2006; Naveau et al., 2007; Parnell, 2011), following an approach previously developed (Blard et al., 2013; Martin et al., 2018). In practice, we first computed a synthetic probability density function (pdf) for each moraine, summing the individual pdf of all individual ^{36}Cl ages f_{Sample}:

$$f_{Moraine}(t) = \frac{1}{n}\sum_{i=1}^{n} f_{Sample} \quad (1)$$

Then, the pdf of ages of moraines that are in successive stratigraphic order were processed using Bayesian filtering. Including these stratigraphic observations permitted to refine the pdf of both younger and older moraines, considering that a distal moraine is necessarily older than a proximal one (Martin et al., 2018). Filtered pdf, f^* of older and younger moraines, are computed according to Equations (2) and (3), respectively:

$$f^*_{Older\ Moraine}(t) = f_{Older\ Moraine}(t) \times \int_0^t f_{Younger\ Moraine}(\tau)d\tau \quad (2)$$

$$f^*_{Younger\ Moraine}(t) = f_{Younger\ Moraine}(t) \times \int_t^\infty f_{Older\ Moraine}(\tau)d\tau \quad (3)$$

This filtering is useful to reduce the total dating uncertainties arising from geological dispersions (erosion or inheritance). In practice, the vicinity of the successive moraines of this dataset implied that this filtering was only applied to moraines V1 and V2 of Val Travers (this study; Fig. 3) and moraines M1 and M2 of Ampere (^{36}Cl ages were first published in Jomelli et al. (2017) and Verfaillie et al. (2021); Fig. 5). It was indeed unnecessary to apply this filtering to other moraine couples, because the corresponding ^{36}Cl ages are too distant.

3.4. Review of existing Holocene cosmogenic data

We aim to compare the updated Kerguelen glacial chronologies to those from other southern mid-latitude regions. To address this issue, we focused on studies devoted to alpine glaciers, from the alpine ICE-D database (http://alpine.ice-d.org/), which compiles cosmogenic nuclide exposure ages (mostly ^{10}Be) from alpine glacier sites around the world. We preferentially target moraine datasets providing direct dating of the main advances of a glacier. Available data from southern mid-latitude glacier chronologies (n = 14) were tabulated as follows: *(i)* moraine mean ages with their inferred internal uncertainties were attributed to one of the subperiods of the Holocene (Early, Mid- or Late Holocene) based on the nominal age and *(ii)* we only selected the glacial chronologies for which the entire sequence of Holocene moraines in the valley were preserved and dated. After age compilation, we identified patterns according to either the presence or absence of at least one moraine belonging to a specific subperiod in each valley. The results and interpretation of these patterns are presented in Supplementary Material Table 2, 3 and 4 and in Fig. 8. The class of data is shown as qualitative histograms. The x-axis of the histograms represents the three sub periods of the Holocene, namely Early Holocene (11.6–8 ka), Mid-Holocene (8–4 ka) and Late Holocene (4–0 ka). The height of the bar represents the qualitative appreciation of the length of the glacier following the stratigraphic principle.

4. Results and age interpretation

4.1. ^{36}Cl ages from Val Travers site (n = 10)

Samples VLT-10, -11, −12 and −13 from V1 moraine give ages of 12.6 ± 1.7 ka, 16.0 ± 2.1 ka, 16.7 ± 2.2 ka and 14.9 ± 2.0 ka respectively and yield a median age of 16.0 ± 1.9 ka after the Bayesian filtering process, (n = 4). (Table 4, Figs. 3, Fig. 4). ^{36}Cl ages of VLT-05, -06, −07, −08 and −09, collected on V2 moraine are 15.6 ± 2.0 ka, 12.4 ± 1.6 ka, 12.4 ± 1.5 ka, 16.7 ± 2.0 ka and 13.5 ± 1.7 ka, respectively. The median age and total uncertainty of V2 moraine is 12.9 ± 1.7 ka (n = 5) (Table 4, Figs. 3, Fig. 4). The ^{36}Cl age of VLT-04, which was extracted from a bedrock atop the U-shaped valley is 17.3 ± 2.2 ka (Table 4, Fig. 4).

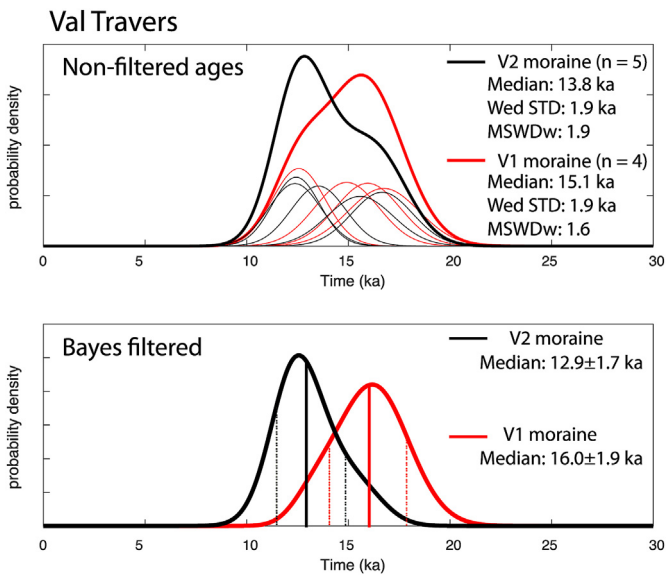

Fig. 3. Probability plots of ^{36}Cl boulder CRE ages from V1 (red curves) and V2 (black curves) moraines at Val Travers site before the Bayesian filter (upper panel) and after the Bayesian filter (bottom panel). Individual ages are represented by Gaussian curves in the upper panel, which only include the analytical uncertainties. The summed probability is presented by thick curves. Also shown are the statistical parameters for each landform. (For interpretation of the references to color in this figure legend, the reader is referred to the Web version of this article.)

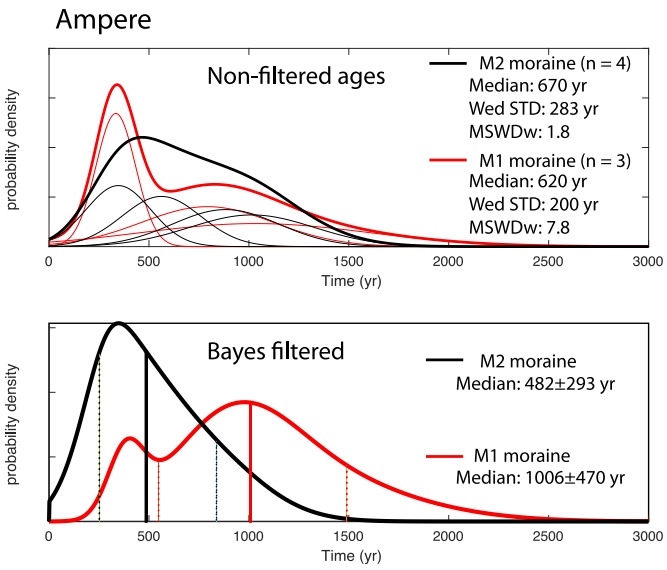

Fig. 5. Probability plots of ^{36}Cl boulder CRE ages from M1 (red curves) and M2 (black curves) moraines at Ampere site (^{36}Cl boulder CRE ages were first published in Jomelli et al. (2017) and Verfaillie et al. (2021)) before the Bayesian filter (upper panel) and after the Bayesian filter (bottom panel). Individual ages are represented by Gaussian curves in the upper panel, which only include the analytical uncertainties. The summed probability is presented by thick curves. Also shown are the statistical parameters for each landform. (For interpretation of the references to color in this figure legend, the reader is referred to the Web version of this article.)

4.2. ^{36}Cl ages from Ampere Glacier site (n = 11)

The erratic boulder samples associated with bedrock surfaces, MO-12, -11, −04, −03, −08 and −06, yield ages of 290 ± 140 yr, 870 ± 180 yr, 80 ± 50 yr, 680 ± 340 yr, 620 ± 170 yr and 2.37 ± 0.38 ka, respectively (Table 4, Fig. 6). MO-04 and -06 were identified as outliers based on the Chi^2 test and were therefore excluded from the mean age calculation. MO-04 has an age considered too young probably due to post-depositional rotation or exhumation, whereas the older age of MO-06 is probably affected by inheritance. The remaining samples MO-12, -11, −03 and −06 have a mean arithmetic age of 610 ± 250 yr. The bedrock samples MO-13, -05, −02, −09 and −07 taken from downstream to upstream on the right shore of Ampere Lake yield ages of 11.3 ± 1.6 ka, 14.0 ± 1.8 ka, 10.1 ± 1.3 ka, 4.43 ± 0.59 ka and 8.9 ± 1.1 ka (Table 4, Fig. 6). The interpretation of these ages will be discussed in section 5.1. Individual moraine boulder ^{36}Cl ages presented in Fig. 6 were first published in Jomelli et al. (2017) and Verfaillie et al. (2021). The weighted means of M1 and M2 moraines and associated total uncertainties gave ages of 800 ± 260 yr and 580 ± 310, respectively.

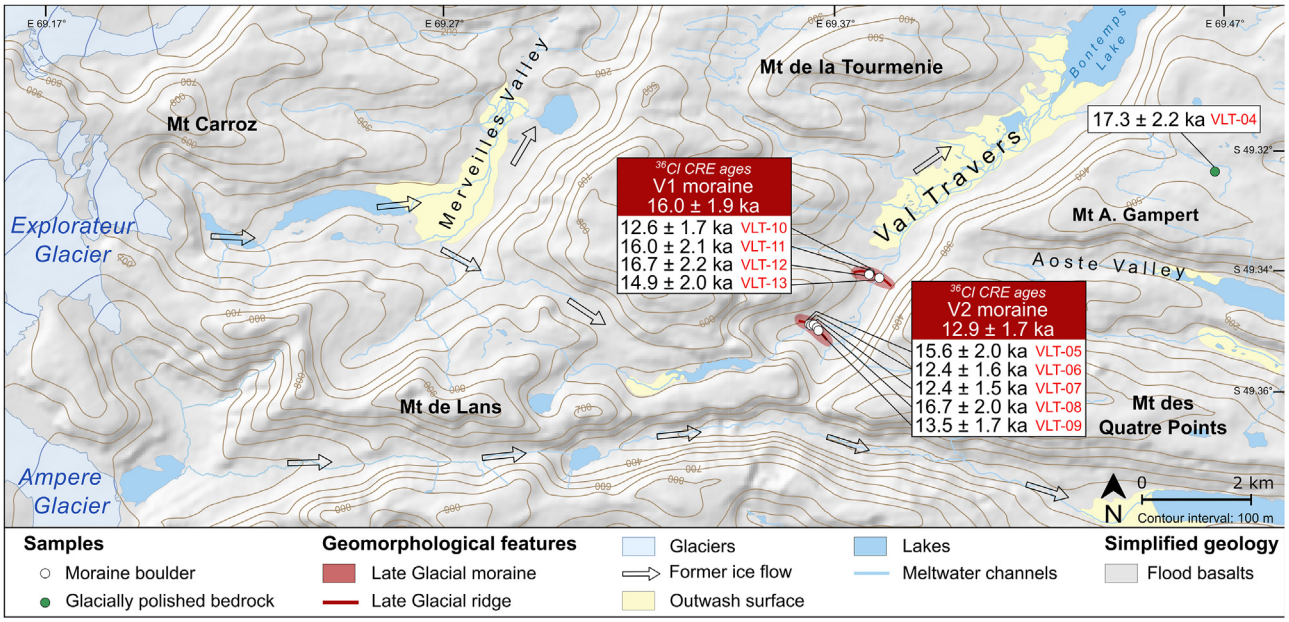

Fig. 4. Glacial geomorphological map of the Val Travers site. White boxes show the ^{36}Cl sample ages of moraine and bedrock with their analytical uncertainties. The median ages for moraine groups are shown in colored boxes with their total uncertainties (i.e. standard deviation, analytical and production rate uncertainties).

After the Bayesian filtering process, M1 moraine gives a median age of 1000 ± 470 yr (n = 3) and M2 moraine gives a median age of 480 ± 290 yr (n = 4) (Fig. 5).

4.3. ^{36}Cl ages (n = 13), ^{10}Be ages (n = 3) and ^{26}Al/^{10}Be ratios (n = 2) from Arago Glacier site

At the Arago Glacier sampling site, we dated three moraines, one bedrock surface and three erratic boulders. The outermost A1 moraine, composed of syenites, was dated using ^{36}Cl on feldspar separates from all samples, and ^{10}Be and ^{26}Al on quartz of two samples. The bedrock surface (RDB-13), which was also sampled from a syenite, was dated only with ^{10}Be and ^{26}Al on quartz. Finally, the two innermost moraines A2a-b, composed of trachytes and syenites, were dated with ^{36}Cl on whole rock and feldspar separates.

The ^{36}Cl surface exposure ages at the Arago Glacier site range from 760 ± 150 yr to 15.4 ± 3.1 ka (Table 4, Fig. 7) and moraine ages are in agreement with their stratigraphic position. The ^{36}Cl ages RDB-01, -02, −04 and −05 of the outermost (oldest) A2a moraine are 760 ± 150 yr, 1.38 ± 0.23 ka, 2.25 ± 0.44 ka and 1.21 ± 0.23 ka, respectively. RDB-04 is probably affected by nuclide inheritance and is rejected as an outlier. The arithmetic mean of the remaining ages of A2a moraine and total uncertainty are 1.12 ± 0.33 ka (n = 3).

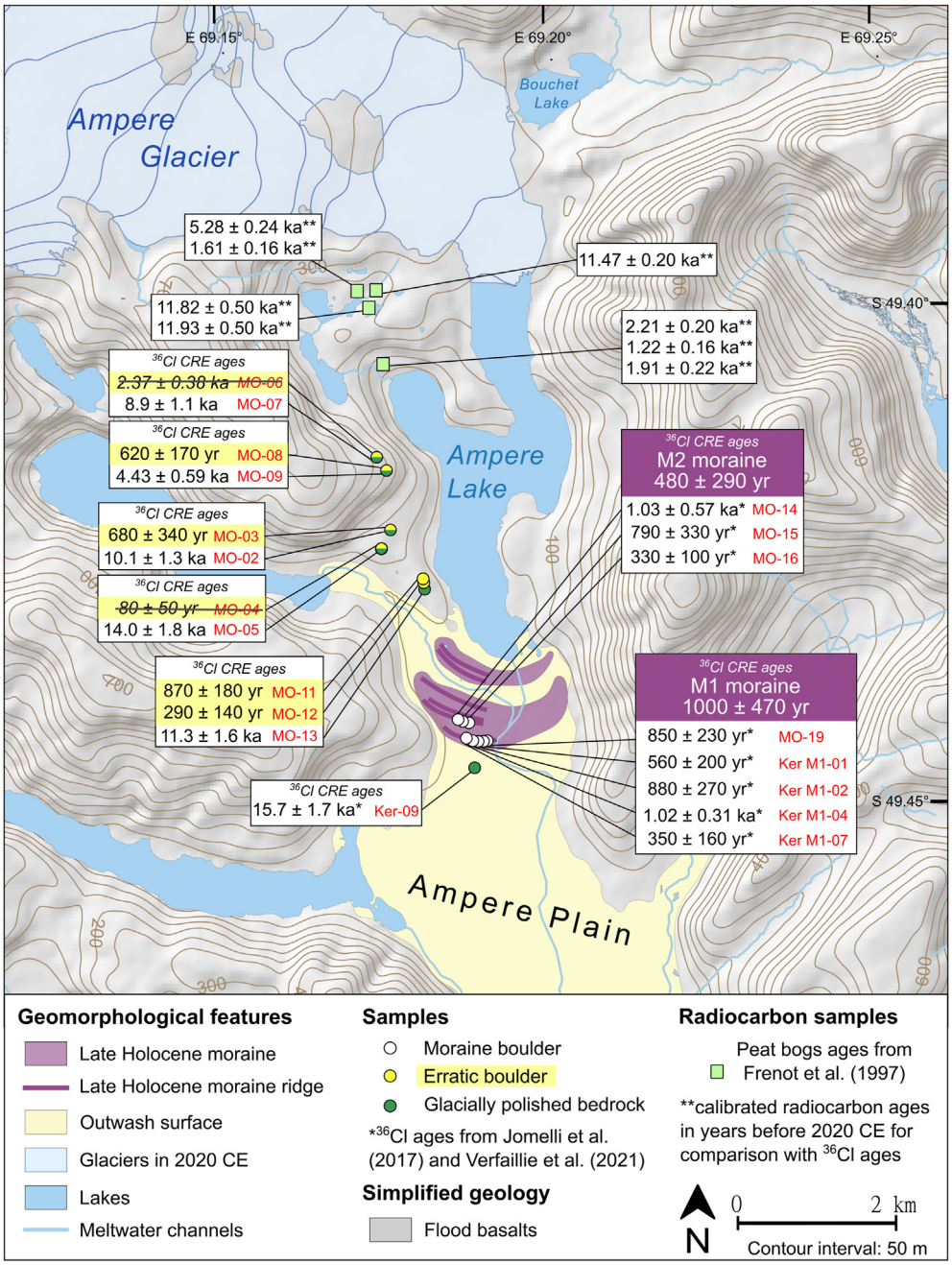

Fig. 6. Glacial geomorphological map of the Ampere Glacier. White boxes show the ^{36}Cl sample ages of erratic boulders and bedrock with their inferred analytical uncertainties. Samples written in striked-through italic text are rejected as outliers and therefore excluded from the discussion. Moraine boulder ^{36}Cl CRE ages are from Jomelli et al. (2017) and Verfaillie et al. (2021). The median ages for moraine groups are shown in colored boxes with their total uncertainties (i.e. standard deviation, analytical and production rate uncertainties). Radiocarbon ages in cal BP are presented in Jomelli et al. (2017).

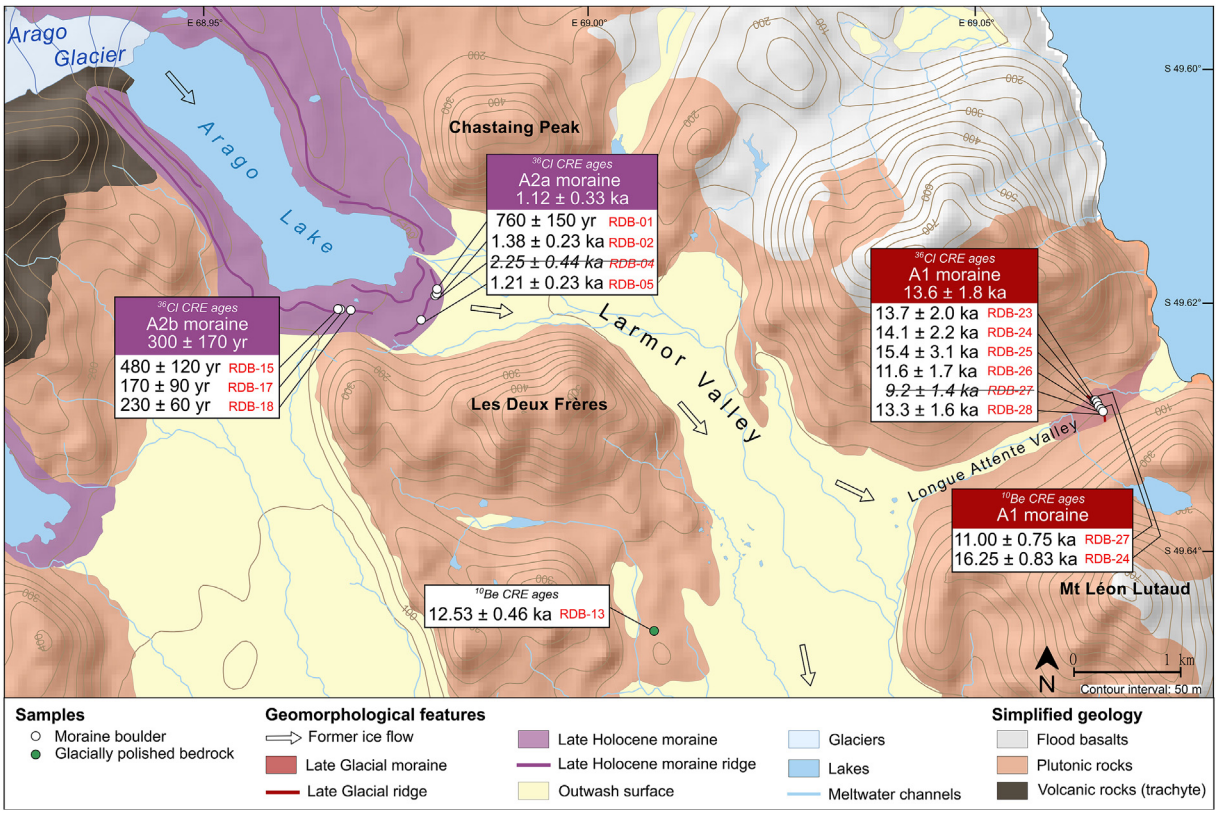

Fig. 7. Glacial geomorphological map of the Arago Glacier site. White boxes show ^{36}Cl and ^{10}Be sample ages of moraine boulders and bedrock with their inferred analytical uncertainties. Samples written in striked-through italic text are rejected as outliers and therefore excluded from the discussion. The arithmetic means for moraine groups are shown in colored boxes with their total uncertainties (i.e. standard deviation, analytical and production rate uncertainties).

On the innermost (youngest) A2b moraine, samples RDB-15, -17 and −18 give ^{36}Cl ages of 480 ± 120, 170 ± 90, 230 ± 60 yr and the moraine has a mean age of 300 ± 170 yr.

Near Les Deux Frères (in between A1 moraine and A2a-b moraine complex; Fig. 7), the bedrock sample RDB-13, collected in syenites upstream of A1 moraine, yields a ^{10}Be age of 12.53 ± 0.46 ka and a ^{26}Al/^{10}Be ratio of 6.48 ± 0.64 (Table 5), which is consistent with the ^{26}Al/^{10}Be production ratio of 6.75 calculated by Balco and Rovey (2008) and Balco et al. (2008). This age suggests that this bedrock sample has been continuously exposed at the surface and does not contain any isotopic inheritance from the last interglacial stadial.

Samples RDB-23, -24, −25, −26, −27 and −28, which were collected on the top of the outermost (oldest) A1 moraine have individual ages of 13.7 ± 2.0 ka, 14.1 ± 2.2 ka, 15.4 ± 3.1 ka, 11.6 ± 1.7 ka, 9.2 ± 1.4 ka and 13.3 ± 1.6 ka, respectively. RDB-24 and -27 yield ^{10}Be ages of 16.25 ± 0.83 and 11.00 ± 0.75 ka, respectively (Table 5, Fig. 7). No statistical difference can be observed between ^{10}Be CRE ages and ^{36}Cl CRE ages of these two samples (Tables 4 and 5). The ^{10}Be and ^{36}Cl CRE ages of sample RDB-27 are both the lowest in the whole age population and have to be related to the high RDB-27 ^{26}Al/^{10}Be ratio of 9.42 ± 1.41 that may indicate that this surface might have been exposed at depth and then re-expose at surface when recently exhumed (Akçar et al., 2017). Therefore, both ^{10}Be and ^{36}Cl CRE ages are considered as outliers. The ^{26}Al measurement of RDB-24 did not yield a meaningful result probably due to analytical issues and is therefore not considered further. The mean ^{36}Cl age for the A1 moraine, excluding RDB-27, is 13.6 ± 1.8 ka (n = 5).

5. Discussion

5.1. Timing of glacier fluctuations at Kerguelen Archipelago since the Late Glacial

Spanning from ~17,000–~70 years, this new surface exposure dataset improves our knowledge on the Kerguelen glacier fluctuations during the Late Glacial period and the Holocene (Figs. 4, 6 and 7).

^{36}Cl dating of a bedrock sample (VLT-04) at an altitude of 437 m a.s.l. at the Val Travers site, suggests that this location became ice free at 17.3 ± 2.2 ka ago (Fig. 4). This finding is consistent with previous ages from erratics at the Presqu'île de la Grye (mean age of 19.8 ± 2.2 ka) located about 10 km east of Val Travers but at an altitude of about 70 m a.s.l. (Jomelli et al., 2017). These results indicate that during the beginning of the Late Glacial period a general deglaciation was occurring (at least in this sector east of CIC).

At the bottom of the adjacent valley, a branch of Explorateur glacier deposited the V1 moraine at 16.0 ± 1.9 ka ago, likely during the Heinrich Stadial 1 (HS1; 17.5–14.7 ka; Rasmussen et al., 2014). However, considering the high uncertainty from this V1 mean moraine age (1.9 ka), it cannot be excluded that this moraine was instead deposited during the beginning of the ACR. In any case, this new data provides another evidence of main glacier extent during this period on the archipelago, as the Belvedere moraine has already been dated to the HS1/ACR period (15.5 ± 1.8 ka) on the southwest of the archipelago (Jomelli et al., 2018). Upstream in Val Travers another moraine deposition (moraine V2) occurred at 12.9 ± 1.7 ka ago. Within the calculated uncertainties, this moraine

age is consistent with previous observations near Presqu'île de la Grye, where the Bontemps moraine was formed northeast of the Val Travers site 13.6 ± 1.5 ka ago by the advance of the Explorateur Glacier (Jomelli et al., 2017, 2018). On Rallier du Baty Peninsula, the A1 moraine of Arago Glacier may have been formed during the same period at 13.6 ± 1.8 ka ago. Another small debris-covered glacier (Gentil Glacier) located south of the archipelago on the Gallieni Peninsula, also experienced glacial advances that occurred at 14.3 ± 2.3 ka (Charton et al., 2020). All these earlier dated moraines are indistinguishable within the calculated range of uncertainties with the new age of V2 moraines at Val Travers and the A1 moraine at Rallier du Baty peninsula. Altogether, these data suggest that during the phase of deglaciation that had started earlier than about 20 ka, glaciers of the archipelago stagnated or readvanced at least once.

Interestingly, no evidence of Early nor Mid-Holocene glacier extents has been found so far, suggesting that glaciers were smaller at Kerguelen during these periods than they were during the Late Holocene re-advances (Frenot et al., 1997; Jomelli et al., 2017; Charton et al., 2020). These Late-Holocene re-advances are corroborated by new evidence at two sites. One such site is the proglacial margin of Arago Glacier (Fig. 7), where the A2a moraine is dated to the last millennium (1.12 ± 0.33 ka ago). Several moraine ridges upstream of A2a moraine, including the A2b moraine, that was deposited 300 ± 170 yr ago, attest to further glacier advances or stillstands within the last millennium. Given the absence of moraines between A1 (Late Glacial) and A2a moraines, it is assumed that the glacier generally receded to at least this location between the end of the Late Glacial period and the Late Holocene advance. In addition, the bedrock sample (RDB-13) located on the proglacial margin of the Arago Glacier in between A1 and A2a-b moraines is dated at 12.53 ± 0.46 ka ago, which suggests that this area has been ice free since at least 13 ka.

In Ampere Glacier's forefield, the oldest Holocene advance is recorded by the outermost M1 moraine and, after Bayesian filtering, is now dated at 1000 ± 470 yr ago (1110 ± 470 CE). A subsequent advance led to the formation of the M2 moraine, which is now dated at 480 ± 290 yr ago (1590 ± 290 CE) (Fig. 6). These findings are complemented by ^{36}Cl dating of erratic boulders perched on glacially-polished bedrock surfaces on the right-lateral proglacial margin of the Ampere Glacier located ~2–4 km upstream and ~90–250 m higher than the M2 moraine. The erratic boulder samples yield a mean age of ~ 610 yr (Fig. 6), which is indistinguishable from the mean ages of M1 and M2. The prolongation of these aligned boulders can geometrically be connected with the moraine sequence that M1 and M2 are part of (Fig. 6). Therefore, it is very likely that they represent the former ice margin that can be related with the formation of one or several of these last-millennium-moraines. Five of the erratic boulders are paired with glacially-polished bedrock surface samples, with the goal to constrain the timing of deglaciation and detect potential periods of successive exposure and burial, indicated by nuclide inheritance in the bedrock surfaces (e.g. Fabel et al., 2002). The bedrock surfaces at this location were apparently exposed for durations that range between ~14 ka and ~4 ka. The apparent ^{36}Cl CRE ages of the bedrock being systematically older than those of the erratic boulders (mean age ~ 610 yr), confirm a complex history of bedrock exposure, meaning that the surfaces contain nuclide inheritance from one or several periods of exposure that pre-date the last-millennium-advances. Given that the apparent bedrock exposure durations do not exceed ~14 ka and that evidence elsewhere from the Kerguelen Islands shows large glacier extents still at ~14 ka and before, we hypothesize the following exposure-burial scenario. Substantial ice cover during the last glacial cycle eroded these locations deeply enough to remove any cosmogenic nuclide inventories that might have accumulated during previous warm periods; following the retreat from the last large glacier extents of the ACR (at ~14 ka), the sample locations experienced deglaciation and ^{36}Cl started to accumulate continuously until 1 ka. At this stage, the Ampere Glacier re-advanced and covered these locations again until (latest) ~150 yr ago, as approximately suggested by the nearby moraine sequence and the erratic boulders located on these bedrock surfaces. During this last-millennium-ice-cover, the glacier eroded the subglacial bedrock surfaces and thus reduced the ^{36}Cl inventory accumulated between ~14 ka and 1 ka. Varying erosion rates as a function of topography and related ice velocity led to variable nuclide reduction at the five bedrock surface locations, thus explaining the range of apparent bedrock exposure durations. Following this scenario, a first-order estimate indicates that a uniform subglacial erosion (=abrasion) rate of ~1 mm/yr (corresponding to an abrasion depth of ~85 cm during the ~850 yr of ice cover) can explain the apparent exposure duration of the sample with the lowest ^{36}Cl inventory (MO-09; ~4.4 ka), whereas sample MO-05 (~14.0 ka) would not have been eroded. Besides abrasion, deep plucking of bedrock is a common subglacial erosion process that can explain variable Holocene cosmogenic nuclide inventories in nearby bedrock surfaces (Rand and Goehring, 2019). Holocene subglacial erosion rates between 0.02 and > 1.8 mm/yr have been inferred in crystalline forefields of Alpine glaciers, based on cosmogenic multi-nuclide methods (Goehring et al., 2011; Schimmelpfennig et al., 2022). Rates of between 0 and ~1 mm/yr in volcanic (less hard) rocks and the warm-based glacier setting in Kerguelen seem realistic to explain the apparent variable bedrock exposure durations and the proposed exposure-burial scenario. We consider the possibility of significant ^{36}Cl inventories inherited from earlier warm periods at these locations unlikely, as no evidence of such warm periods during the last glacial cycle has been provided so far. In addition, significant discrepancies between paired exposure ages of erratics and glacially-polished bedrock elsewhere on Kerguelen may also be expected if nuclide inheritance is a general concern in this setting, like in cold-based glacier sites (Nichols et al., 2019). However, other existing ^{36}Cl dates of glacially-polished bedrock on the islands are in good agreement with nearby erratics and/or the general deglaciation trend for this region since MIS 3 (Jomelli et al., 2017, 2018). This scenario thus suggests that the new bedrock surfaces investigated in this study were ice-free for most of the Holocene period and provide new evidence that the Kerguelen glaciers had a little extent during most of the Early and Mid-Holocene.

5.2. Comparison with other paleoglacial records within the southern mid-latitude region

The updated ^{36}Cl dataset consolidates earlier data regarding the Kerguelen glacier chronologies since the Late Glacial, and it also provides new chronological evidence that the Kerguelen glacier behavior followed a different Holocene pattern compared to other regions in the southern mid-latitudes.

Our dataset suggests a possible glacier advance (or stillstand long enough to create a moraine) during HS1 like in Rakaia valley in New Zealand, where glaciers experienced a stillstand at ~16 ka in their global recession trend (Putnam et al., 2013). This is at odds with observations from other southern mid-latitude regions where a global recession of glaciers is generally recorded (e.g. Hall et al., 2013). Our dataset also indicates a glacier advance during the ACR, in agreement with findings from other southern mid-latitude regions (e.g. Putnam et al., 2010a; Pedro et al., 2015; Darvill et al., 2016; Graham et al., 2017). Regarding the Holocene, we performed a review of published moraine CRE ages of glaciers located in Patagonia, New Zealand, Antarctic Peninsula and South Georgia,

using the alpine ICE-D database (Balco, 2020) (Fig. 8). Detailed information is available in supplemental material Table 2, 3 and 4. Based on this evaluation, we identified the following three different patterns of glacial evolution in this region of the southern mid-latitudes during the Holocene period (Fig. 8):

(i). The first pattern, named type-A (glacier sites n = 5), corresponds to a decreasing glacial extent throughout the Holocene, evidenced by several Early, Mid-and Late Holocene moraines dated in numerous glacial valleys. Consequently, glaciers experienced their maximum Holocene advance at the beginning of this period, and then progressively retreated until present-day. Glaciers following the A-type evolution are located in New-Zealand (Putnam et al., 2012), north of 50°S in Patagonia (Reynhout et al., 2019), and South Georgia (Bakke et al., 2021).

(ii). The second pattern, type-B (glacier sites n = 5), corresponds to small glacial extents during the Early Holocene, glacier re-advances during the Mid- Holocene and glacier recession during the Late Holocene. These moraines exhibit progressively smaller glacier extents, which are dated to the Mid- and Late Holocene only, and provide evidence of severe glacier retreat during the Early Holocene. Glaciers following this trend are located in Patagonia between ~50°S and 55°S (Kaplan et al., 2016) and in the Antarctic Peninsula (Kaplan et al., 2020 and references therein).

(iii). The last pattern, type-C (glacier sites n = 4), is mainly based on what has been documented so far at Kerguelen. According to the currently available estimates, glaciers were smaller throughout the Early to Mid-Holocene than during their maximum Late Holocene extent. Hitherto, the only other location in the Southern Hemisphere where this atypical pattern has been suggested is in southernmost Patagonia (>55°S) (Reynhout et al., 2021 and references therein).

5.3. Assessing potential climate drivers of glacier oscillations in Kerguelen Archipelago during the Late Glacial and Holocene

The patterns discussed in section 5.2. provide three regionally contrasting Holocene glacier evolutions within the southern mid-latitude region suggesting complex glacier climatic relationships

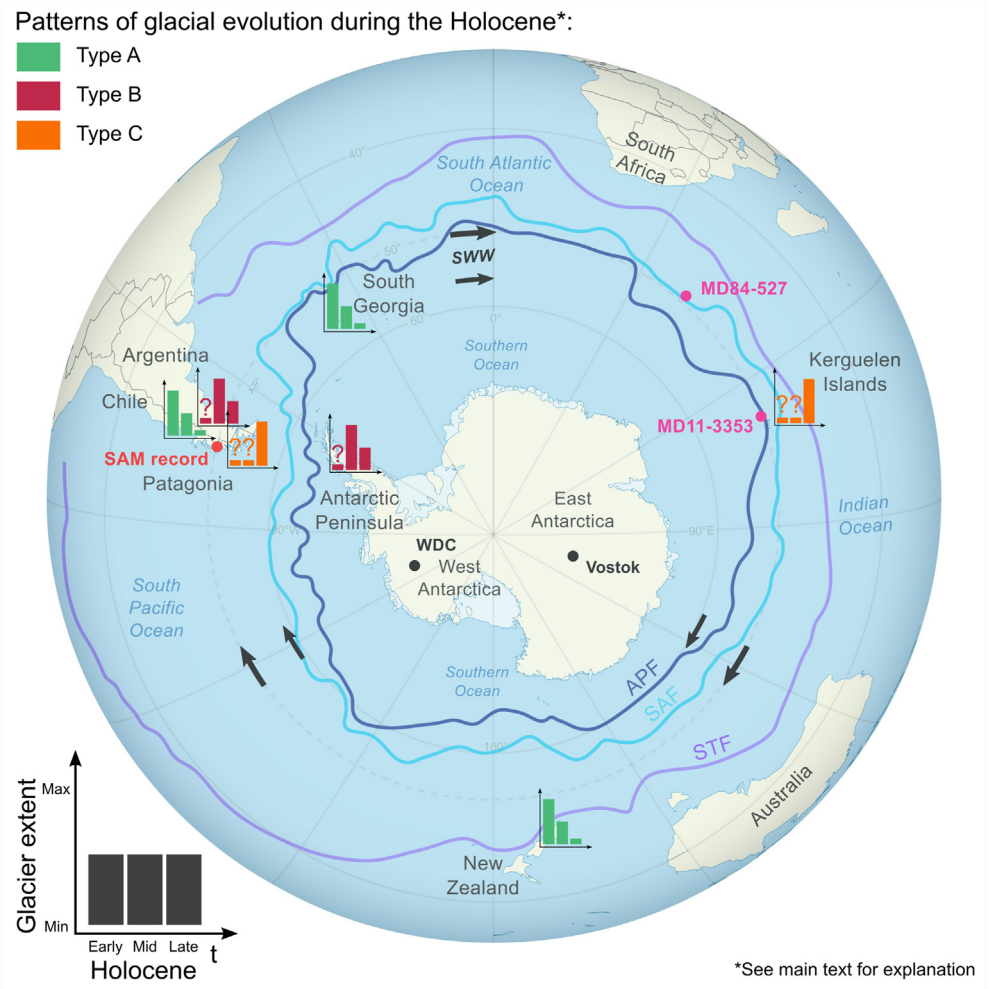

Fig. 8. Different qualitative patterns of glacial evolution within the southern mid-latitudes during the Holocene. Legend information is explained in sections 3.4 and 5.2. The x-axis bar of the histograms represents the subperiods of the Holocene (Early Holocene, Mid-Holocene and Late Holocene), whereas the y-axis bar represents the qualitative appreciation of glacier length (see section 3.4). The question marks above the histogram bars represent missing moraines belonging to the referred period in the glacial valley. The black arrow shows the modern position of the Southern Westerly Winds (SWW, ~50–60°S), the dark blue line provides a representation of the modern Antarctic Polar Front (APF), the light blue line is the sub-Antarctic Front (SAF) and the purple line is the sub-Tropical Front (STF). Also shown in pink dots are the positions of the marine cores, black dots depict the locations of the ice cores and the single red dot provides the location of the Southern Annular Mode record discussed in section 5.3. (For interpretation of the references to color in this figure legend, the reader is referred to the Web version of this article.)

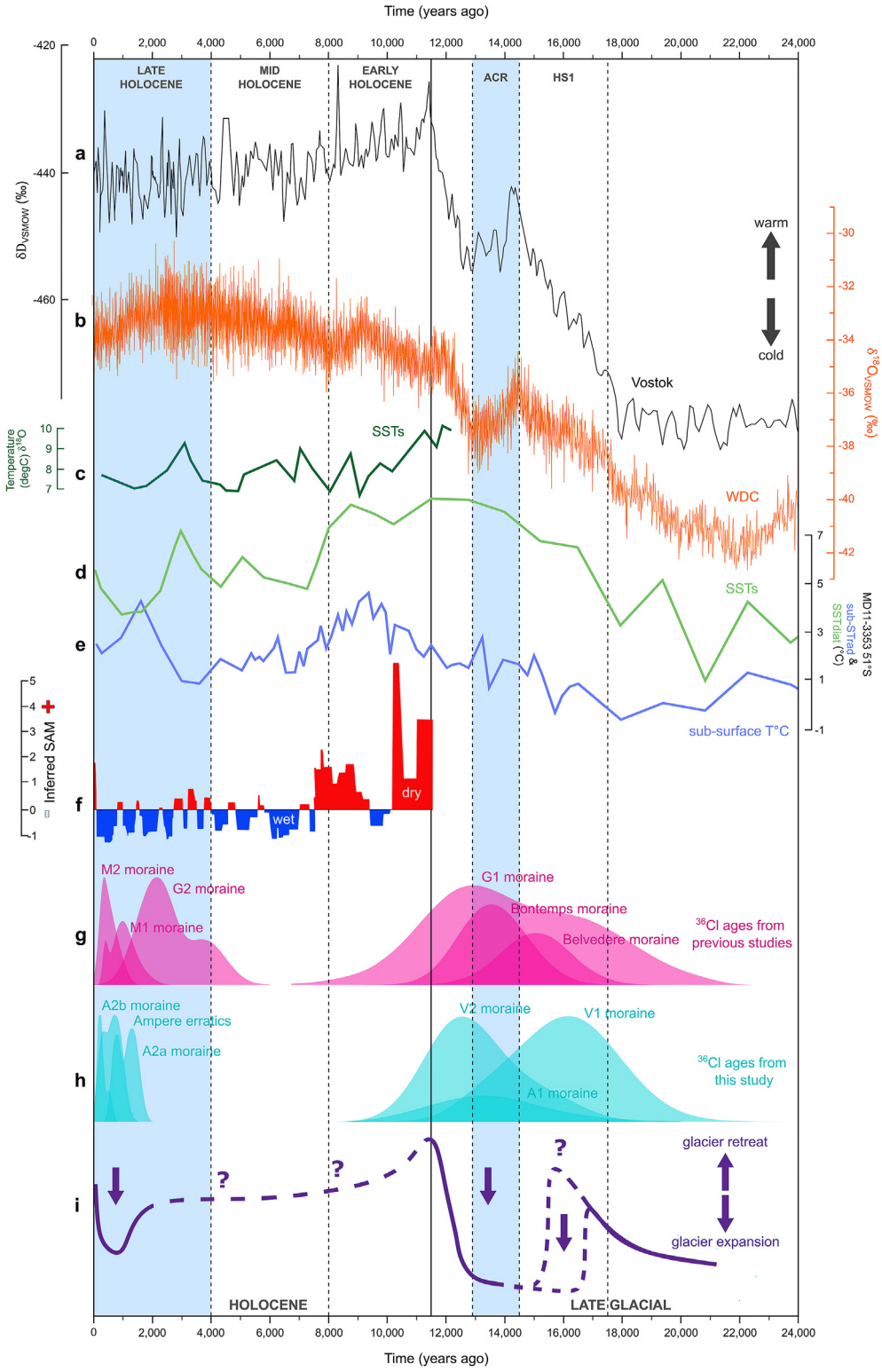

Fig. 9. Comparison of Kerguelen paleoglacier records with Antarctic and southern mid-latitude climatic proxies (locations are shown in Fig. 8). Proxies for atmospheric temperature fluctuations are **a.** δD_{VSMOW} (black curve) from Vostok (East Antarctica; Petit et al., 1999) and **b.** $\delta^{18}O_{VSMOW}$ (orange curve) from West Antarctica (WAIS Divide Project Members, 2013). **c.** is the SST reconstruction from $\delta^{18}O$ on planktonic foraminifera (green curve) from MD84-527 marine core, compiled by Kauffman et al. (2020) but first published by Pichon et al. (1992). **d.** is the reconstructed subsurface temperatures and **e.** the SSTs, both from the MD11-3353 core (51°S; Civel-Mazens et al., 2021). **f.** is the Inferred SAM-like index reconstruction for the Holocene period as shaded boxes (red = positive and blue = negative) from Lago Cipreses non-arboreal pollen in Patagonia (Moreno et al., 2018). Also shown are the ^{36}Cl CRE age probability density distributions with their analytical uncertainties only during the Late Glacial and the Holocene periods from Kerguelen of **g.** previous studies (Jomelli et al., 2017, 2018; Charton et al., 2020; Verfaillie et al., 2021) and **h.** this study. Finally, **i.** is a schematic evolution of Kerguelen glacier extents. (For interpretation of the references to color in this figure legend, the reader is referred to the Web version of this article.)

at a regional scale in the southern mid-latitudes that need to be further explored. Here, we do not address the underlying potential climatic puzzle within the whole southern mid-latitude region but focus on climatic conditions that may have driven glacier fluctuations at Kerguelen (Fig. 9).

We suspect paleoglacier variations at Kerguelen to be strongly impacted by the combined influence of sea surface temperatures (SSTs) variations and precipitation changes related to the position of the westerlies, which is partly driven by the SAM. Since air and sea surface temperatures are significantly correlated at Kerguelen (Favier et al., 2016), paleo SSTs data around Kerguelen should be more relevant for local temperatures, than remote Antarctic ice core records. Moreover, reconstructed SSTs combined with subsurface temperatures from the core MD11-3353 (Fig. 9d and e) located southwest of Kerguelen make it also possible to document latitudinal changes in the position of the oceanic fronts (Civel-Mazens et al., 2021).

As variations of the SAM and the latitudinal gradient of SSTs are not necessarily in phase through time, they may have acted or not in the same direction on paleoglacier behavior. The impacts of negative phases of the SAM (SAM-) (more precipitation) and cold SSTs would favor a positive mass balance while the effects of a SAM- and warm SSTs would partly compensate for each other.

Below, we explore links between these two climate drivers and glacier patterns throughout the Late Glacial and Holocene. Forcings controlling glacier behavior on Kerguelen remain particularly puzzling for the Late Glacial as precipitation changes and the SAM index for this period remain unknown. Our dataset reveals a general deglaciation trend interrupted by at least one glacier advance or stillstand either during HS1 and/or during the ACR. Assuming an advance or a stillstand during HS1, it would have occurred concomitantly with cold, but warming, atmospheric conditions recorded in Antarctica (Petit et al., 1999; WAIS Divide Project Members, 2013, Fig. 9a and b). If occurring during the ACR, it would have been concordant with the cooling recorded from the Antarctic ice cores (Petit et al., 1999; WAIS Divide Project Members, 2013, Fig. 9a and b) and elsewhere in the Southern Ocean (Pedro et al., 2015). We note that warm SSTs seemingly prevailed at that time, as indicated by core MD11-3353 (Fig. 9d), suggesting that the APF and the SAF were already, and remained, at a more southern latitude. However, the SST record presents very low resolution over the deglaciation, and other SST records suggest the ACR was regionally expressed (Labracherie et al., 1989; Ai et al., 2020; Orme et al., 2020; Civel et al., 2021). The subsurface temperature record in core MD11-3353 conversely shows a plateau during the ACR in agreement with air temperature evolution and glacier standstill. During the ACR, increased moisture input has been reported at the Kerguelen Archipelago, based on multi-proxy analyses of peat sequences (van der Putten et al., 2015). This might be due to a potential northward shift of the SWW during this period and might explain a positive glacier mass balance due to enhanced precipitation. This concept is supported by intensified wet conditions documented from different proxy records in Patagonia (Davies et al., 2020) suggesting that the SWW were centered at ~50°S during the ACR, while the modern SWW belt lies between 50°S and 60°S (Garreaud et al., 2009).

During the Holocene a reconstruction of precipitation changes attributed to SAM variations offers a good opportunity to analyze the influence of the centennial-to-millennial expression of this climate mode on glacier dynamics at Kerguelen. So far, only one precipitation-SAM reconstruction spanning the Early to Late Holocene exists, and is inferred from the Lago Cipreses non-arboreal pollen (NAP) record in Patagonia (51°S) (Moreno et al., 2018, Fig. 9f). According to this record, SAM is mostly characterized by positive-state-like SAM conditions (less precipitation at the latitude of Kerguelen) during the Early Holocene, i.e. from ~11.5 to ~10.2 ka, and during the so called 'Early Warm Dry Anomaly', from ~9.5 to 7.5 ka, which is in agreement with warm and dry climate conditions from the Kerguelen Islands inferred from a multi-proxy analyses on a peat record (reconstruction of wind strength, humidity and relative temperature) investigated by van der Putten et al. (2015). In addition, the Holocene trend of reconstructed SSTs (Kauffman et al., 2020) near Kerguelen in the Southern Indian Ocean (shown in Fig. 9c) and southwest of Kerguelen (Civel-Mazens et al., 2021; shown in Fig. 9d) reveals warmer SSTs during the Early Holocene. Altogether dry conditions, in response to pervasive SAM + like conditions, and rather warm SSTs in the region would explain the relatively small glacier extents at the Kerguelen Archipelago during the Early Holocene.

We notice a cold excursion of SSTs in the Mid-Holocene. Moraines from that time have not yet been identified. Yet, glaciers might have advanced during the Mid-Holocene, but their moraines may have been obliterated by the more extensive Late Holocene glacier advances. However, this potential Mid-Holocene advance may not have lasted long because of the multi-millennial ages of the sampled glacially-polished bedrock, which indicate extensive deglaciation.

During the Late Holocene, negative-state-like SAM conditions increased (Fig. 9f), suggesting enhanced precipitation, which, combined with rather cold SSTs in the region (Fig. 9c–e), would have favored glacier re-advance on the Kerguelen Archipelago.

6. Conclusion

This study aimed to better constrain the evolution of glaciers on the Kerguelen Archipelago, using *in situ*-produced ^{36}Cl CRE dating from moraine boulders, erratic and glacially-polished bedrock collected on forefields of the Arago Glacier, Ampere Glacier and in the Val Travers Valley. Evidence of a Late Glacial glacier advance at the Val Travers site at ~16 ka and ~12.9 ka and at the Arago Glacier at ~13.6 is provided, which can likely be related to the HS1 and ACR cold spells. While the finding of the HS1 advance is infrequent, the ACR advance is consistent with previous results from other locations on the archipelago, and more generally in the southern mid-latitude region, suggesting that glaciers experienced a broadly synchronous behavior during the ACR.

Early and Mid-Holocene glacio-geomorphic features that are testament to glacier advances have not yet been found on the archipelago. In addition, CRE dating of paired erratic boulders (~610 yr) and glacially-polished bedrock surfaces (with exposure duration of up to 14 ka) at the Ampere site indicate that this proglacial margin was ice free for several millennia during the Holocene period. These results, when combined with previously published radiocarbon-dated peat ages, suggest that the Ampere Glacier was in a retracted position during most of the Holocene. The new ages also enable refinement of the glacial chronology for Kerguelen and reveal new Late Holocene advances, at ~1.12 ka and ~300 yr at the Arago Glacier site and at ~1 ka and ~430 yr at the Ampere Glacier site. These findings suggest that Kerguelen glaciers retreated significantly after their (large) ACR extents and were smaller than their last-millennium-extents for most of the Holocene. The data also indicates that the glaciers only re-advanced again from ~1 ka. This implies that any moraines potentially formed during Early and Mid-Holocene were obliterated by the more extensive Late Holocene glacier extents.

To compare this trend with the glacier evolution in other southern mid-latitude regions, a review of *in situ* cosmogenic data was performed. Three different glacier patterns were identified within the southern mid-latitudes, implying that glacier/climate relationships across this region need further investigations. In the

Kerguelen region, a rise in nearby SSTs and a decrease in precipitation, owing to a latitudinal shift of the SWW could explain the relatively smaller extent of Kerguelen glaciers during the Early Holocene. On the contrary, decreasing SSTs and increased precipitation during the Mid- and Late Holocene may have led to glacier expansion in the case of Kerguelen.

Author contributions

VJ, GD, DV, VF, VR, DG and CL conducted the fieldwork on the islands. JC, IS, VJ and GD participated in producing the cosmogenic data. GA, DB and KK (ASTER Team) performed accelerator mass spectrometry measurements. JC, IS, VJ, GD, PHB, RB, LM interpreted the cosmogenic ages; JC, VJ, IS and PHB prepared the figures. All authors contributed to writing the paper.

Declaration of competing interest

The authors declare that they have no known competing financial interests or personal relationships that could have appeared to influence the work reported in this paper.

Acknowledgments

This work has received financial support from the LabEx DynamiTe (ANR-11-LABX-0046) Les Envahisseurs as part of the 'Investissements d'Avenir' programme. This paper was also supported by the French INSU LEFE Glacepreker project and by the IPEV Kesaaco 1048 project. The ^{36}Cl, ^{10}Be and ^{26}Al measurements were performed at the ASTER national accelerator mass spectrometry facility (CEREGE, Aix-en-Provence) that is supported by the INSU/CNRS, the ANR through the 'Projets thématiques d'excellence' programme for the 'Equipements d'excellence' ASTER-CEREGE action and IRD. We are very thankful for the compositional analyses at SARM/CRPG (Nancy, France). We also acknowledge the work of Fatima Mokadem, Laëtitia Léanni and Valery Guillou, who helped processing data.

Appendix A. Supplementary data

Supplementary data to this article can be found online at https://doi.org/10.1016/j.quascirev.2022.107461.

References

Ai, X.E., Studer, A.S., Sigman, D.M., Martínez-García, A., Fripiat, F., Thöle, L.M., Michel, E., Gottschalk, J., Arnold, L., Moretti, S., Schmitt, M., Oleynik, S., Jaccard, S.L., Haug, G.H., 2020. Southern Ocean upwelling, Earth's obliquity, and glacial-interglacial atmospheric CO2 change. Science 370 (6522), 1348–1352. https://doi.org/10.1126/science.abd2115.

Akçar, N., Ivy-Ochs, S., Alfimov, V., Schlunegger, F., Claude, A., Reber, R., Christl, M., Vockenhuber, C., Dehnert, A., Rahn, M., Schluchter, C., 2017. Isochron-burial dating of glaciofluvial deposits: first results from the Swiss Alps. Earth Surf. Process. Landforms 42, 2414–2425.

Anjar, J., Akçar, N., Larsen, E.A., Lyså, A., Marrero, S., Mozafari, N., Vockenhuber, C., 2021. Cosmogenic exposure dating (36Cl) of landforms on Jan mayen, north Atlantic, and the effects of bedrock formation age assumptions on 36Cl ages. Geosciences 11, 390. https://doi.org/10.3390/geosciences11090390.

Annell, H., 2005. Petrology and Geochemistry of the 25 Ma Mt. Marion Dufresne Basaltic Section on the Kerguelen Archipelago: Constraining the Transition from Tholeiitic to Mildly Alkalic Volcanism on a Major Oceanic Island. Master of Science – MSc. University of British Columbia, Canada. https://doi.org/10.14288/1.0052331.

Arnold, M., Merchel, S., Bourles, D., Braucher, R., Benedetti, L., Finkel, R.C., Aumaître, G., Gottdang, A., Klein, M., 2010. The French accelerator mass spectrometry facility ASTER: improved performance and developments. Nucl. Instrum. Method Phys. Res. B: Beam Interact. Mater. Atoms 268, 1954–1959. https://doi.org/10.1016/j.nimb.2010.02.107.

Bakke, J., Paasche, Ø., Schaefer, J., Timmermann, A., 2021. Long-term demise of sub-Antarctic glaciers modulated by the Southern Hemisphere Westerlies. Sci. Rep. 11, 8361. https://doi.org/10.1038/s41598-021-87317-5.

Balco, G., Rovey, C.W., 2008. An isochron method for cosmogenic-nuclide dating of buried soils and sediments. Am. J. Sci. 308 (10), 1083–1114. https://doi.org/10.2475/10.2008.02.

Balco, G., Stone, J.O., Lifton, N.A., Dunai, T.J., 2008. A complete and easily accessible means of calculating surface exposure ages or erosion rates from 10Be and 26Al measurements. Quat. Geochronol. 3 (3), 174–195. https://doi.org/10.1016/j.quageo.2007.12.001.

Balco, G., 2020. Technical note: a prototype transparent-middle-layer data management and analysis infrastructure for cosmogenic-nuclide exposure dating. Geochronol. Discuss 1–10. https://doi.org/10.5194/gchron-2020-6.

Berthier, E., Bris, R. le, Mabileau, L., Testut, L., Rémy, F., 2009. Ice wastage on the Kerguelen islands (49°S, 69°E) between 1963 and 2006. J. Geophys. Res. Earth Surf. 114, 1–11. https://doi.org/10.1029/2008JF001192.

Blard, P.-H., Braucher, R., Lave, J., Bourles, D., 2013. Cosmogenic 10Be production rate calibrated against 3He in the high Tropical Andes (3800-4900 m, 20-22°S). Earth Planet Sci. Lett. 382, 140–149. https://doi.org/10.1016/j.epsl.2013.09.010.

Braucher, R., Guillou, V., Bourles, D., Arnold, M., Aumaître, G., Keddadouche, K., Nottoli, E., 2015. Preparation of ASTER in-house 10Be/9 Be standard solutions. Nucl. Instrum. Method Phys. Res. B: Beam Interact. Mater. Atoms 361, 335–340. https://doi.org/10.1016/j.nimb.2015.06.012.

Charton, J., Jomelli, V., Schimmelpfennig, I., Verfaillie, D., Favier, V., Mokadem, F., Gilbert, A., Brun, F., Aumaître, G., Bourlès, D.L., Keddadouche, K., 2020. A debris-covered glacier at Kerguelen (49°S, 69°E) over the past 15 000 years. Antarct. Sci. 33 (1), 103–115. https://doi.org/10.1017/S0954102020000541.

Chmeleff, J., von Blanckenburg, F., Kossert, K., Jakob, D., 2010. Determination of the 10Be half-life by multicollector ICP-MS and liquid scintillation counting. Nucl. Instrum. Method Phys. Res. B: Beam Interact. Mater. Atoms 268 (2), 192–199. https://doi.org/10.1016/j.nimb.2009.09.012.

Civel-Mazens, M., Crosta, X., Cortese, G., Michel, E., Mazaud, A., Ther, O., Ikehara, M., Itaki, T., 2021. Impact of the agulhas return current on the oceanography of the Kerguelen Plateau region, Southern Ocean, over the last 40 kyrs. Quat. Sci. Rev. 251, 106711. https://doi.org/10.1016/j.quascirev.2020.106711.

Cooley, D., Naveau, P., Jomelli, V., Rabatel, A., Grancher, D., 2006. A bayesian hierarchical extreme value model for lichenometry. Environmetrics 17, 555–574.

Darvill, C.M., Bentley, M.J., Stokes, C.R., Shulmeister, J., 2016. The timing and cause of glacial advances in the southern mid-latitudes during the last glacial cycle based on a synthesis of exposure ages from Patagonia and New Zealand. Quat. Sci. Rev. 149, 200–214. https://doi.org/10.1016/j.quascirev.2016.07.024.

Davies, B.J., Darvill, C.M., Lovell, H., Bendle, J.M., Dowdeswell, J.A., Fabel, D., García, J.L., Geiger, A., Glasser, N.F., Gheorghiu, D.M., Harrison, S., Hein, A.S., Kaplan, M.R., Martin, J.R.V., Mendelova, M., Palmer, A., Pelto, M., Rodés, Á., Sagredo, E.A., Smedley, R.K., Smellie, J.L., Thorndycraft, V.R., 2020. The evolution of the Patagonian Ice Sheet from 35 ka to the present day (PATICE). Earth Sci. Rev. 204, 103152. https://doi.org/10.1016/j.earscirev.2020.103152.

Delunel, R., Bourlès, D.L., van der Beek, P.A., Schlunegger, F., Leya, I., Masarik, J., Paquet, E., 2014. Snow shielding factors for cosmogenic nuclide dating inferred from long-term neutron detector monitoring. Quat. Geochronol. 24, 16–26. https://doi.org/10.1016/j.quageo.2014.07.003.

Dosso, L., Vidal, P., Cantagrel, J.-M., Lameyre, J., Marot, A., Zimine, S., 1979. Kerguelen: continental fragment or oceanic island: petrology and isotopic geochemistry evidence. Earth Planet Sci. Lett. 43, 46–60.

Dunai, T.J., Binnie, S.A., Hein, A.S., Paling, S.M., 2014. The effects of a hydrogen-rich ground cover on cosmogenic thermal neutrons: implications for exposure dating. Quat. Geochronol. 22, 183–191. https://doi.org/10.1016/j.quageo.2013.01.001.

Eaves, Shaun R., Winckler, Gisela, Mackintosh, Andrew N., Schaefer, Joerg M., Townsend, Dougal B., Doughty, Alice M., Jones, Selwyn R., Leonard, Graham S., 2019. Late-glacial and Holocene glacier fluctuations in North Island, New Zealand. Quat. Sci. Rev. 223. https://doi.org/10.1016/j.quascirev.2019.105914.

Fabel, D., Stroeven, A.P., Harbor, J., Kleman, J., Elmore, D., Fink, D., 2002. Landscape preservation under Fennoscandian ice sheets determined from in situ produced ^{10}Be and ^{26}Al. Earth Planet. Sci. Lett. 201 (2), 397–406. https://doi.org/10.1016/S0012-821X(02)00714-8.

Favier, V., Verfaillie, D., Berthier, E., Menegoz, M., Jomelli, V., Kay, J.E., Ducret, L., Malbéteau, Y., Brunstein, D., Gallée, H., Park, Y.H., Rinterknecht, V., 2016. Atmospheric drying as the main driver of dramatic glacier wastage in the southern Indian Ocean. Sci. Rep. 6, 1–12. https://doi.org/10.1038/srep3239.

Fink, D., Vogt, S., Hotchkis, M., 2000. Cross-sections for 36Cl from Ti at Ep = 35-150 MeV: applications to in-situ exposure dating. Nucl. Instrum. Method Phys. Res. B: Beam Interact. Mater. Atoms 172, 861–866. https://doi.org/10.1016/S0168-583X(00)00200-7.

Frenot, Y., Gloaguen, J.C., van de Vijver, B., Beyens, L., 1997. Datation de quelques sediments tourbeux holocènes et oscillations glaciaires aux îles Kerguelen. Comptes Rendus l'Academie Sci. 320, 567–573. https://doi.org/10.1016/S0764-4469(97)84712-9.

Garreaud, R.D., Vuille, M., Compagnucci, R., Marengo, J., 2009. Present-day south American climate. Palaeogeogr. Palaeoclimatol. Palaeoecol. 281, 180–195.

Giret, A., Weis, D., Grégoire, M., Mattielli, N., Moine, B., Michon, G., Scoates, J., Tourpin, S., Delpech, G., Gerbe, M.-C., Doucet, S., Ethien, R., Cottin, J.-Y., 2003. L'archipel des Kerguelen: les plus vieilles îles dans le plus jeune océan. Geologues 15–23.

Goehring, B.M., Schaefer, J.M., Schluechter, C., Lifton, N.A., Finkel, R.C., Jull, A.J.T., Akçar, N., Alley, R.B., 2011. The Rhone Glacier was smaller than today for most of the Holocene. Geology 39 (7), 679–682. https://doi.org/10.1130/G32145.1.

Gosse, J.C., Phillips, F.M., 2001. Terrestrial in situ cosmogenic nuclides: theory and

application. Quat. Sci. Rev. 20 (14), 1475–1560. https://doi.org/10.1016/S0277-3791(00)00171-2.
Graham, A.G.C., Kuhn, G., Meisel, O., Hillenbrand, C.D., Hodgson, D.A., Ehrmann, W., Wacker, L., Wintersteller, P., dos Santos Ferreira, C., Römer, M., White, D., Bohrmann, G., 2017. Major advance of South Georgia glaciers during the Antarctic Cold Reversal following extensive sub-Antarctic glaciation. Nat. Commun. 8, 1–15. https://doi.org/10.1038/ncomms14798.
Hall, B.L., Porter, C.T., Denton, G.H., Lowell, T.V., Bromley, G.R.M., 2013. Extensive recession of Cordillera Darwin glaciers in southernmost south America during Heinrich stadial 1. Quat. Sci. Rev. 62, 49–55. https://doi.org/10.1016/j.quascirev.2012.11.026.
Hall, B.L., Lowell, T.V., Bromley, G.R.M., Denton, G.H., Putnam, A.E., 2019. Holocene glacier fluctuations on the northern flank of Cordillera Darwin, southernmost South America. Quat. Sci. Rev. 222, 105904. https://doi.org/10.1016/j.quascirev.2019.105904.
Ivy-Ochs, S., Synal, H.A., Roth, C., Schaller, M., 2004. Initial results from isotope dilution for Cl and 36Cl measurements at the PSI/ETH Zurich AMS facility. Nucl. Instrum. Method Phys. Res. B: Beam Interact. Mater. Atoms 223–224, 623–627. https://doi.org/10.1016/j.nimb.2004.04.115.
Jomelli, V., Mokadem, F., Schimmelpfennig, I., Chapron, E., Rinterknecht, V., Favier, V., Verfaillie, D., Brunstein, D., Legentil, C., Michel, E., Swingedouw, D., Jaouen, A., Aumaitre, G., Bourlès, D.L., Keddadouche, K., 2017. Sub-Antarctic glacier extensions in the Kerguelen region (49°S, Indian Ocean) over the past 24,000 years constrained by 36Cl moraine dating. Quat. Sci. Rev. 162, 128–144. https://doi.org/10.1016/j.quascirev.2017.03.010.
Jomelli, V., Schimmelpfennig, I., Favier, V., Mokadem, F., Landais, A., Rinterknecht, V., Brunstein, D., Verfaillie, D., Legentil, C., Aumaitre, G., Bourlès, D.L., Keddadouche, K., 2018. Glacier extent in sub-Antarctic Kerguelen archipelago from MIS 3 period: evidence from 36Cl dating. Quat. Sci. Rev. 183, 110–123. https://doi.org/10.1016/j.quascirev.2018.01.008.
Kaplan, M.R., Strelin, J.A., Schaefer, J.M., Denton, G.H., Finkel, R.C., Schwartz, R., Putnam, A.E., Vandergoes, M.J., Goehring, B.M., Travis, S.G., 2011. In-situ cosmogenic 10Be production rate at Lago Argentino, Patagonia: implications for late-glacial climate chronology. Earth Planet Sci. Lett. 309 (1–2), 21–32. https://doi.org/10.1016/j.epsl.2011.06.018.
Kaplan, M.R., Schaefer, J.M., Strelin, J.A., Denton, G.H., Anderson, R.F., Vandergoes, M.J., Finkel, R.C., Schwartz, R., Travis, S.G., Garcia, J.L., Martini, M.A., Nielsen, S.H.H., 2016. Patagonian and southern south Atlantic view of Holocene climate. Quat. Sci. Rev. 141, 112–125. https://doi.org/10.1016/j.quascirev.2016.03.014.
Kaplan, M.R., Strelin, J.A., Schaefer, J.M., Peltier, C., Martini, M.A., Flores, E., Winckler, G., Schwartz, R., 2020. Holocene glacier behavior around the northern Antarctic Peninsula and possible causes. Earth Planet Sci. Lett. 534, 116077. https://doi.org/10.1016/j.epsl.2020.116077.
Kaufman, D.S., McKay, N.P., Routson, C.C., Erb, M., Davis, B.A.S., Heiri, O., Jaccard, S., Tierney, J.E., Dätwyler, C., Axford, Y., Brussel, T., Cartapanis, O., Chase, B.M., Dawson, A., de Vernal, A., Engels, S., Jonkers, L., Marsicek, J., Moffa-Sánchez, P., Morrill, C., Orsi, A., Rehfeld, K., Saunders, K., Sommer, P.S., Thomas, E., Tonello, M., Tóth, M., Vachula, R., Andreev, A., Bertrand, S., Biskaborn, B., Bringué, M., Brooks, S., Caniupán, M., Chevalier, M., Cwynar, L., Emile-Geay, J., Fegyveresi, J., Feurdean, A., Finsinger, W., Fortin, M.-C., Foster, L., Fox, M., Gajewski, K., Grosjean, M., Hausmann, S., Heinrichs, M., Holmes, N., Ilyashuk, B., Ilyashuk, E., Juggins, S., Khider, D., Koinig, K., Langdon, P., Larocque-Tobler, I., Li, J., Lotter, A., Luoto, T., Mackay, A., Magyari, E., Malevich, S., Mark, B., Massaferro, J., Montade, V., Nazarova, L., Novenko, E., Pařil, P., Pearson, E., Peros, M., Pienitz, R., Płóciennik, M., Porinchu, D., Potito, A., Rees, A., Reinemann, S., Roberts, S., Rolland, N., Salonen, S., Self, A., Seppä, H., Shala, S., St-Jacques, J.-M., Stenni, B., Syrykh, L., Tarrats, P., Taylor, K., van den Bos, V., Velle, G., Wahl, E., Walker, I., Wilmshurst, J., Zhang, E., Zhilich, S., 2020. A global database of Holocene paleotemperature records. Sci. Data 7, 1–34. https://doi.org/10.1038/s41597-020-0445-3.
Korschinek, G., Bergmaier, A., Faestermann, T., Gerstmann, U.C., Knie, K., Rugel, G., Wallner, A., Dillmann, I., Dollinger, G., von Gostomski, C.L., Kossert, K., Maiti, M., Poutivtsev, M., Remmert, A., 2010. A new value for the half-life of 10Be by Heavy-Ion Elastic Recoil Detection and liquid scintillation counting. Nucl. Instrum. Method Phys. Res. B: Beam Interact. Mater. Atoms 268 (2), 187–191. https://doi.org/10.1016/j.nimb.2009.09.020.
Labracherie, M., Labeyrie, L.D., Duprat, J., Bard, E., Arnold, M., Pichon, J.-J., Duplessy, J.-C., 1989. The last deglaciation in the Southern Ocean. Paleoceanogr. Paleoclimatol. 4 (6), 629–638. https://doi.org/10.1029/PA004i006p00629.
Marrero, S.M., Phillips, F.M., Caffee, M.W., Gosse, J.C., 2016. CRONUS-Earth cosmogenic 36Cl calibration. Quat. Geochronol. 31, 199–219. https://doi.org/10.1016/j.quageo.2015.10.002.
Martin, L., Blard, P.-H., Balco, G., Lave, J., Delunel, R., Lifton, N., Laurent, V., 2017. The CREp program and the ICE-D production rate calibration database: a fully parameterizable and updated online tool to compute cosmic-ray exposure ages. Quat. Geochronol. 38 (25–4). https://doi.org/10.1016/j.quageo.2016.11.006.
Martin, L., Blard, P.-H., Lavé, J., Condom, T., Premaillon, M., Jomelli, V., Brunstein, D., Lupker, M., Charreau, J., Mariotti, V., Tibari, B., , ASTER Team, Davy, E., 2018. Lake Tauca Highstand (Heinrich stadial 1) driven by a southward shift of the Bolivian high. Sci. Adv. 4, 1–10. https://doi.org/10.1126/sciadv.aar2514.
Merchel, S., Bremser, W., 2004. First international 26Al interlaboratory comparison - Part I. Nucl. Instrum. Methods Phys. Res. Sect. B Beam Interact. Mater. Atoms 223–224, 393–400. https://doi.org/10.1016/j.nimb.2004.04.076.
Merchel, S., Arnold, M., Aumaître, G., Benedetti, L., Bourlès, D.L., Braucher, R., Alfimov, V., Freeman, S.P.H.T., Steier, P., Wallner, A., 2008. Towards more precise 10Be and 36Cl data from measurements at the 10−14 level: influence of sample preparation. Nucl. Instrum. Method Phys. Res. B: Beam Interact. Mater. Atoms 266 (22), 4921–4926. https://doi.org/10.1016/j.nimb.2008.07.031.
Merchel, S., Bremser, W., Alfimov, V., Arnold, M., Aumaître, G., Benedetti, L., Bourlès, D.L., Caffee, M., Fifield, L.K., Finkel, R.C., Freeman, S.P.H.T., Martschini, M., Matsushi, Y., Rood, D.H., Sasa, K., Steier, P., Takahashi, T., Tamari, M., Tims, S.G., Tosaki, Y., Wilcken, K.M., Xu, S., 2011. Ultra-trace analysis of 36Cl by accelerator mass spectrometry: an interlaboratory study. Anal. Bioanal. Chem. Res. 400, 3125–3132. https://doi.org/10.1007/s00216-011-4979-2.
Moreno, P.I., Vilanova, I., Villa-Martínez, R., Dunbar, R.B., Mucciarone, D.A., Kaplan, M.R., Garreaud, R.D., Rojas, M., Moy, C.M., de Pol-Holz, R., Lambert, F., 2018. Onset and evolution of southern annular mode-like changes at centennial timescale. Sci. Rep. 8, 1–9. https://doi.org/10.1038/s41598-018-21836-6.
Muscheler, R., Beer, J., Kubik, P.W., Synal, H.-A., 2005. Geomagnetic field intensity during the last 60,000 years based on 10Be and 36Cl from the Summit ice cores and 14C. Quat. Sci. Rev. 24 (16–17), 1849–1860. https://doi.org/10.1016/j.quascirev.2005.01.012.
Naveau, P., Jomelli, V., Cooley, D., Grancher, D., Rabatel, A., 2007. Modeling uncertainties in lichenometry studies with an application: the tropical Andes (Charquini Glacier in Bolivia). Arctic Antarct. Alpine Res. 39, 277–288.
Nichols, K.A., Goehring, B.M., Balco, G., Johnson, J.S., Hein, A.S., Todd, C., 2019. New last glacial maximum ice thickness constraints for the Weddell sea embayment, Antarctica. Cryosphere 13, 2935–2951. https://doi.org/10.5194/tc-13-2935-2019, 2019.
Nicolaysen, K., Frey, F.A., Hodges, K.v., Weis, D., Giret, A., 2000. 40Ar/39Ar geochronology of flood basalts from the Kerguelen Archipelago, southern Indian Ocean: implications for Cenozoic eruption rates of the Kerguelen plume. Earth Planet Sci. Lett. 174, 313–328. https://doi.org/10.1016/S0012-821X(99)00271-X.
Orme, L.C., Crosta, X., Miettinen1, A., Divine, D.V., Husum, K., Isaksson, E., Wacker, L., Mohan, R., Ther, O., Ikehara, M., 2021. sea surface temperature in the Indian sector of the Southern Ocean over the late glacial and Holocene. Clim. Past 16, 1451–1467. https://doi.org/10.5194/cp-16-1451-2020.
Park, Y.-H., Durand, I., Kestenare, E., Rougier, G., Zhou, M., d'Ovidio, F., Cotté, C., Lee, J.-H., 2014. Polar Front around the Kerguelen Islands: an up-to-date determination and associated circulation of surface/subsurface waters. J. Geophys. Res.: Oceans 119, 6575–6592. https://doi.org/10.1002/2014JC010061.
Parnell, A.C., Buck, C.E., Doan, T.K., 2011. A review of statistical chronology models for high-resolution, proxy-based Holocene palaeoenvironmental reconstruction. Quat. Sci. Rev. 30, 2948e2960. https://doi.org/10.1016/j.quascirev.2011.07.024.
Pedro, J.B., Bostock, H.C., Bitz, C.M., He, F., Vandergoes, M.J., Steig, E.J., Chase, B.M., Krause, C.E., Rasmussen, S.O., Markle, B.R., Cortese, G., 2015. The spatial extent and dynamics of the Antarctic Cold Reversal. Nat. Geosci. 9, 1–6. https://doi.org/10.1038/ngeo2580.
Petit, J.R., Jouzel, J., Raynaud, D., Barkov, N.I., Barnola, J.M., Basile, I., Bender, M., Chappellaz, J., Davis, M., Delaygue, G., Delmotte, M., Kotiyakov, V.M., Legrand, M., Lipenkov, V.Y., Lorius, C., Pépin, L., Ritz, C., Saltzman, E., Stievenard, M., 1999. Climate and atmospheric history of the past 420,000 years from the Vostok ice core, Antarctica. Nature 399, 429–436. https://doi.org/10.1038/20859.
Phillips, F.M., Plummer, M.A., 1996. CHLOE: a program for interpreting in-situ cosmo- genic nuclide data for surface exposure dating and erosion studies. In: Abstracts of the 7th International Conference on Accelerator Mass Spectrometry, pp. 98–99.
Phillips, F.M., Stone, W.D., Fabryka-Martin, J.T., 2001. An improved approach to calculating low-energy cosmic-ray neutron fluxes near the land/atmosphere interface. Chem. Geol. 175, 689–701. https://doi.org/10.1016/S0009-2541(00)00329-6.
Pichon, J.-J., Labeyrie, L.D., Bareille, G., Labracherie, M., Duprat, J., Jouzel, J., 1992. Surface water temperature changes in the high latitudes of the southern hemisphere over the last glacial-interglacial cycle. Paleoceanography 7, 289–318.
Ponthus, L., 2018. Origine, évolution et mise en place d'un pluton récent en contexte intraplaque océanique. Exemple du complexe sud de Rallier du Baty, Kerguelen (T.A.A.F.). Ph.D. thesis. Université Toulouse 3 Paul Sabatier, France.
Ponthus, L., de Saint Blanquat, M., Guillaume, D., Le Romancer, M., Pearson, N., O'Reilly, S.Y., Grégoire, M., 2020. Plutonic processes in transitional oceanic plateau crust: structure, age and emplacement in the South Rallier du Baty laccolith, Kerguelen Islands. Terra. Nova 32, 408–414.
Putnam, A.E., Denton, G.H., Schaefer, J.M., Barrell, D.J.A., Andersen, B.G., Finkel, R.C., Schwartz, R., Doughty, A.M., Kaplan, M.R., Schlüchter, C., 2010a. glacier advance in southern middle-latitudes during the Antarctic cold reversal. Nat. Geosci. 3, 700–704. https://doi.org/10.1038/ngeo962.
Putnam, A.E., Schaefer, J.M., Barrell, D.J.A., Vandergoes, M., Denton, G.H., Kaplan, M.R., Finkel, R.C., Schwartz, R., Goehring, B.M., Kelley, S.E., 2010b. In situ cosmogenic 10Be production-rate calibration from the Southern Alps, New Zealand. Quat. Geochronol. 5 (4), 392–409. https://doi.org/10.1016/j.quageo.2009.12.001.
Putnam, A.E., Schaefer, J.M., Denton, G.H., Barrell, D.J.A., Finkel, R.C., Andersen, B.G., Schwartz, R., Chinn, T.J.H., Doughty, A.M., 2012. Regional climate control of glaciers in New Zealand and Europe during the pre-industrial Holocene. Nat. Geosci. 5, 1–4. https://doi.org/10.1038/ngeo1548.

Putnam, A.E., Schaefer, J.M., Denton, G.H., Barrell, D.J.A., Andersen, B.G., Koffman, T.N.B., Rowan, A.V., Finkel, R.C., Rood, D.H., Schwartz, R., Vandergoes, M.J., Plummer, M.A., Brocklehurst, S.H., Kelley, S.E., Ladig, K.L., 2013. Warming and glacier recession in the Rakaia valley, southern Alps of New Zealand, during Heinrich stadial 1. Earth Planet Sci. Lett. 382, 98–110. https://doi.org/10.1016/j.epsl.2013.09.005.

Rand, C., Goehring, B., 2019. The distribution and magnitude of subglacial erosion on millennial timescales at Engabreen, Norway. Ann. Glaciol. 60 (80), 73–81. https://doi.org/10.1017/aog.2019.42.

Rasmussen, S.O., Bigler, M., Blockley, S.P., Blunier, T., Buchardt, S.L., Clausen, H.B., Cvijanovic, I., Dahl-Jensen, D., Johnsen, S.J., Fischer, H., Gkinis, V., Guillevic, M., Hoek, W.Z., Lowe, J.J., Pedro, J.B., Popp, T., Seierstad, I.K., Steffensen, J.P., Svensson, A.M., Vallelonga, P., Vinther, B.M., Walker, M.J.C., Wheatley, J.J., Winstrup, M., 2014. A stratigraphic framework for abrupt climatic changes during the Last Glacial period based on three synchronized Greenland ice-core records: refining and extending the INTIMATE event stratigraphy. Quat. Sci. Rev. 106, 14–28. https://doi.org/10.1016/j.quascirev.2014.09.007.

Raup, B., Racoviteanu, A., Khalsa, S.J.S., Helm, C., Armstrong, R., Arnaud, Y., 2007. The GLIMS geospatial glacier database: a new tool for studying glacier change. Global Planet. Change 56. https://doi.org/10.1016/j.gloplacha.2006.07.018.

Reynhout, S.A., Sagredo, E.A., Kaplan, M.R., Aravena, J.C., Martini, M.A., Moreno, P.I., Rojas, M., Schwartz, R., Schaefer, J.M., 2019. Holocene glacier fluctuations in Patagonia are modulated by summer insolation intensity and paced by Southern Annular Mode-like variability. Quat. Sci. Rev. 220, 178–187. https://doi.org/10.1016/j.quascirev.2019.05.029.

Reynhout, S., Kaplan, M., Sagredo, E., Aravena, J., Soteres, R., Schwartz, R., Schaefer, J., 2021. Holocene glacier history of northeastern Cordillera Darwin, southernmost South America (55°S). Quat. Res. 105, 1–16. https://doi.org/10.1017/qua.2021.45.

Rudolph, E.M., Hedding, D.W., Fabel, D., Hodgson, D.A., Gheorghiu, D.M., Shanks, R., Nel, W., 2020. Early glacial maximum and deglaciation at sub-Antarctic Marion Island from cosmogenic 36Cl exposure dating. Quat. Sci. Rev. 231. https://doi.org/10.1016/j.quascirev.2020.106208.

Sarıkaya, M.A., Çiner, A., Zreda, M., Şen, E., Ersoy, O., 2018. Chlorine degassing constrained by cosmogenic 36Cl and radiocarbon dating of early Holocene rhyodacitic lava domes on Erciyes stratovolcano, central Turkey. J. Volcanol. Geoth. Res. 369, 263–275. https://doi.org/10.1016/j.jvolgeores.2018.11.029.

Schimmelpfennig, I., 2009. Cosmogenic 36Cl in Ca and K Rich Minerals: Analytical Developments, Production Rate Calibrations and Cross Calibration with 3He and 21Ne. Ph.D. thesis. Université Paul Cézanne - Aix-Marseille III, France.

Schimmelpfennig, I., Benedetti, L., Finkel, R., Pik, R., Blard, P.H., Bourlès, D., Burnard, P., Williams, A., 2009. Sources of in-situ 36Cl in basaltic rocks. Implications for calibration of production rates. Quat. Geochronol. 4, 441–461. https://doi.org/10.1016/j.quageo.2009.06.003.

Schimmelpfennig, I., Benedetti, L., Garreta, V., Pik, R., Blard, P.H., Burnard, P., Bourlès, D., Finkel, R., Ammon, K., Dunai, T., 2011. Calibration of cosmogenic 36Cl production rates from Ca and K spallation in lava flows from Mt. Etna (38°N, Italy) and Payun Matru (36°S, Argentina). Geochem. Cosmochim. Acta 75, 2611–2632. https://doi.org/10.1016/j.gca.2011.02.013.

Schimmelpfennig, I., Schaefer, J.M., Putnam, A.E., Koffman, T., Benedetti, L., Ivy-Ochs, S., Schlüchter, C., Arnold, M., Aumaître, G., Bourlès, D., Keddadouche, K., 2014. 36Cl production rate from K-spallation in the European Alps (Chironico landslide, Switzerland). J. Quat. Sci. 29, 407–413. https://doi.org/10.1002/jqs.2720.

Schimmelpfennig, I., Schaefer, J., Lamp, J., Godard, V., Schwartz, R., Bard, E., Tuna, T., Akçar, N., Schlüchter, C., Zimmerman, S.R., ASTER Team, 2022. Glacier response to Holocene warmth inferred from in situ 10Be and 14C bedrock analyses in Steingletscher's forefield (central Swiss Alps). Clim. Past 18, 23–44. https://doi.org/10.5194/cp-18-23-2022.

Solomina, O.N., Bradley, R.S., Jomelli, V., Geirsdottir, A., Kaufman, D.S., Koch, J., McKay, N.P., Masiokas, M., Miller, G., Nesje, A., Nicolussi, K., Owen, L.A., Putnam, A.E., Wanner, H., Wiles, G., Yang, B., 2016. Glacier fluctuations during the past 2000 years. Quat. Sci. Rev. 149, 61–90. https://doi.org/10.1016/j.quascirev.2016.04.008.

Sokolov, S., Rintoul, S.R., 2009. Circumpolar structure and distribution of the Antarctic Circumpolar Current fronts: 2. Variability and relationship to sea surface height. J. Geophys. Res. 114. https://doi.org/10.1029/2008JC005248.

Stone, J.O., 2000. Isotope production. J. Geophys. Res. 105, 753–759.

Stone, J.O., Fifield, K., Vasconcelos, P., 2005. Terrestrial chlorine-36 production from spallation of iron. In: Abstract of 10th International Conference on Accelerator Mass Spectrometry.

Taylor, J.R., 1997. An Introduction to Error Analysis. The Study of Uncertainties in Physical Measurements. University Science Books, Sausalito, USA.

Thompson, D.W.J., Solomon, S., Kushner, P.J., England, M.H., Grise, K.M., Karoly, D.J., 2011. Signatures of the Antarctic ozone hole in Southern Hemisphere surface climate change. Nat. Geosci. 4, 741–749. https://doi.org/10.1038/ngeo1296.

Uppala, S.M., Kållberg, P.W., Simmons, A.J., Andrae, U., Bechtold, V.D.C., Fiorino, M., Gibson, J.K., Haseler, J., Hernandez, A., Kelly, G.A., Li, X., Onogi, K., Saarinen, S., Sokka, N., Allan, R.P., Andersson, E., Arpe, K., Balmaseda, M.A., Beljaars, A.C.M., Berg, L.V.D., Bidlot, J., Bormann, N., Caires, S., Chevallier, F., Dethof, A., Dragosavac, M., Fisher, M., Fuentes, M., Hagemann, S., Hólm, E., Hoskins, B.J., Isaksen, L., Janssen, P.A.E.M., Jenne, R., Mcnally, A.P., Mahfouf, J.-F., Morcrette, J.-J., Rayner, N.A., Saunders, R.W., Simon, P., Sterl, A., Trenberth, K.E., Untch, A., Vasiljevic, D., Viterbo, P., Woollen, J., 2005. The ERA-40 re-analysis. Q. J. R. Meteorol. Soc. 131, 2961–3012. https://doi.org/10.1256/qj.04.176.

van der Putten, N., Verbruggen, C., Björck, S., Michel, E., Disnar, J.R., Chapron, E., Moine, B.N., de Beaulieu, J.L., 2015. The last termination in the south Indian ocean: a unique terrestrial record from Kerguelen islands (49°S) situated within the Southern hemisphere westerly belt. Quat. Sci. Rev. 122, 142–157. https://doi.org/10.1016/j.quascirev.2015.05.010.

Verfaillie, D., Favier, V., Dumont, M., Jomelli, V., Gilbert, A., Brunstein, D., Gallée, H., Rinterknecht, V., Menegoz, M., Frenot, Y., 2015. Recent glacier decline in the Kerguelen Islands (49°S, 69°E) derived from modeling , field observations , and satellite data. J. Geophys. Res. Earth Surf. 120, 637–654. https://doi.org/10.1002/2014JF003329.

Verfaillie, D., Favier, V., Gallée, H., Fettweis, X., Agosta, C., Jomelli, V., 2019. Regional modeling of surface mass balance on the Cook ice cap, Kerguelen islands (49°S, 69°E). Clim. Dynam. 53, 5909–5925. https://doi.org/10.1007/s00382-019-04904-z.

Verfaillie, D., Charton, J., Schimmelpfennig, I., Stroebele, Z., Jomelli, V., Bétard, F., Favier, V., Cavero, J., Berthier, E., Goosse, H., Rinterknecht, V., Legentil, C., Charrassin, R., Aumaître, G., Bourlès, D.L., Keddadouche, K., 2021. Evolution of the Cook Ice Cap (Kerguelen Islands) between the last centuries and 2100 CE based on cosmogenic dating and glacio-climatic modelling. Antarct. Sci. 33 (3), 301–317. https://doi.org/10.1017/S0954102021000080.

WAIS Divide Project Members, 2013. Onset of deglacial warming in West Antarctica driven by local orbital forcing. Nature 500, 440–444. https://doi.org/10.1038/nature12376.

Ward, G.K., Wilson, S.R., 1978. Procedures for comparing and combining radiocarbon age determinations: a critique. Archaeometry 20, 19–31. https://doi.org/10.1111/j.1475-4754.1978.tb00208.x.

Zreda, M.G., Phillips, F.M., Kubik, P.W., Sharma, P., Elmore, D., 1993. Cosmogenic 36Cl dating of young basaltic eruption complex, Lathrop Wells, Nevada. Geology 21, 57–60.

Zweck, C., Zreda, M., Desilets, D., 2013. Snow shielding factors for cosmogenic nuclide dating inferred from Monte Carlo neutron transport simulations. Earth Planet Sci. Lett. 379, 64–71. https://doi.org/10.1016/j.epsl.2013.07.023.